Parameterizations of Reflectance and Effective Emittance for Satellite Remote Sensing of Cloud Properties

PATRICK MINNIS, DONALD P. GARBER, AND DAVID F. YOUNG,

NASA/Langley Research Center, Hampton, Virginia

ROBERT F. ARDUINI

Science Applications International Corporation, Hampton, Virginia

YOSHIHIDE TAKANO

Department of Meteorology, University of Utah, Salt Lake City, Utah

(Revision for *Journal of Atmospheric Science*, October 1997)

ABSTRACT

The interpretation of satellite-observed radiances to derive cloud optical depth and effective particle size requires radiative transfer calculations relating these parameters to the reflectance, transmittance, and emittance of the cloud. Such computations can be extremely time-consuming when used in an operational mode to analyze routine satellite data. Adding-doubling (AD) radiative transfer models are used here to compute reflectance and effective emittance at wavelengths commonly used by operational meteorological satellite imagers for droplet effective radii ranging from 2 to 32 μm and for distributions of randomly oriented hexagonal ice crystals with effective diameters varying from 6 to 135 μm. Cloud reflectance lookup tables were generated at the typical visible-channel wavelength 0.65 μm and the SI) wavelengths, 3.75 and 3.90 μm. A combination of four-point Lagrangian and linear interpolation between the model nodal points is the most accurate and economical method for estimating reflectance as a function of particle size for any set of solar zenith, viewing zenith, and relative azimuth angles. Compared to exact AD calculations, the four-point method retrieves the reflectance to within $\pm$ 3 and 9% for water droplets and ice crystals, respectively. Most of the error is confined to scattering angles near distinct features in a given phase function. The errors are reduced to ~ $\pm$ 2% for ice when the assessment is constrained to only those angles that are actually useful in satellite retrievals. Effective emittance, which includes absorption and scattering effects, was computed at SI;, infrared (IR; 10.7 and 10.8 μm), and split-window (WS; 11.9 and 12.0 μm) wavelengths for a wide range of surface and cloud temperatures using the same ice crystal and water droplet distributions. The results were parameterized with a 32-term polynomial model that depends on the clear-cloud radiating temperature difference, the clear-sky temperature, and viewing zenith angle. A four-point Lagrangian method is used to interpolate between optical depth nodes. The model reproduces the adding-doubling results with an overall accuracy better than $\pm$ 2, 0.4, and 0.3%, respectively, for the SI, IR, and WS emittances, a substantial reduction in the error compared to earlier parameterizations. Temperatures simulated with the emittance models are within 0.6 and 1K for water droplets and ice crystals, respectively, in the SI channels. The IR temperatures are accurate to better than $\pm$0.05K. During the daytime, the simulations of combined reflectance and emittance for the SI channels are as accurate as the emittance models alone except at particular scattering angles. The magnitudes of the errors depend on the angle, particle size, and solar zenith angle. Examples are given showing the parameterizations applied to satellite data. Computational time exceeds that of previous models but the accuracy gain should yield emittances that are more reliable for retrieval of global cloud microphysical properties.

1. Introduction

When integrated over the thickness of a cloud, microphysical properties such as particle phase, shape, and effective size determine the cloud optical depth and ice or liquid water path. These parameters govern the emittance and reflectance of the cloud, and, therefore, ultimately impact the radiation budget and influence climate. The need for understanding the global variability of cloud microphysical properties and their radiative effects has led to the development of several remote sensing techniques for deriving them from satellite-observed radiances. Interpretation of the satellite measurements relies on radiative transfer model calculations to relate a particular set of cloud microphysical characteristics to radiances entering and leaving the top-of-the-atmosphere from a cloud in a

particular direction. The models provide the critical link between the radiance and a physical property.

A variety of spectra have been used to derive cloud microphyiscal properties. Inoue (1985) showed that the differences between the 11.0 and 12.0-μm brightness temperatures observed by the Advanced Very High Resolution Radiometer (AVHRR) could be used to estimate the emittance of optically thin cirrus clouds. The errors in the emittance depended on the sizes of the cloud particles. Parol et al. (1991) found that the 11-12 μm brightness temperature differences are related to the particle size for thin clouds. They also determined that particle shape affects cloud effective emittance. Arking and Childs (1985) developed a method that used the 0.67, 3.7, and 11-μm AVHRR data with models based on Mie calculations of radiance to derive cloud fraction, optical depth, and cloud temperature and to assign a microphysical model. Coakley et al. (1987) and Radke et al. (1989) used the greater 3.7-μm reflectivity of smaller droplets to detect the presence of ship tracks in boundary-layer marine cloudiness. Stone et al. (1990) demonstrated a technique to derive optical depth using paired 3.73 and 10.8-μm AVHRR radiances or matched 3.95 and 12.7-μm Geostationary Operational Environmental Satellite (GOES) data. They inferred particle size by comparing the radiances to calculated brightness temperature differences between the two channels. Han et al. (1994) used near-nadir data from the 0.67, 3.73 and 10.8-μm channels on the AVHRR to derive the effective droplet radii of warm clouds (temperature greater than 0°C) during daytime to provide the first estimates of cloud droplet sizes on a near-global scale.

Until recently, cirrus clouds were assumed to consist of ice spheres in radiative transfer modeling. Cirrus was generally characterized using Mie scattering phase functions, although infinitely long, ice cylinders were occasionally invoked to describe cirrus scattering (e.g., Liou, 1973). With the availability of scattering phase functions for particles shaped more like ice crystals (e.g., Takano and Liou, 1989), it is possible to more accurately model radiances reflected from cirrus clouds. For example, Minnis et al. (1993a) showed that a radiative transfer model employing phase functions for randomly oriented hexagonal ice columns provided a more accurate depiction of the radiance field over cirrus clouds than Mie spheres. They also developed improved parameterizations of infrared cloud emittance by including scattering effects. Baum et al. (1993) demonstrated that radiative transfer calculations of 3.73, 10.8, and 12.0-μm emittances using liquid-water spheres and randomly oriented hexagonal ice columns could explain the AVHRR-observed radiances from single -layer cirrus and stratus and from overlapping cirrus and stratus. Comparison of the calculations and the brightness temperature differences showed that the phase of some midlevel clouds could be determined by ensuring consistency between the data and models for all three channels. While these various efforts are beginning to show improvements in the retrievals of cloud microphysical properties, the advances come at the expense of more complexity and computation time which may limit the operational application of such techniques.

To avoid performing detailed radiative transfer calculations for each satellite scene, it is necessary to reduce the computation time using parameterizations while minimizing loss of accuracy. Rossow et al. (1988) employed a large set of lookup tables describing the angular distribution of reflected visible radiances for clouds having droplets with an effective radius of 10 μm. The lookup tables were computed for clouds having a range of optical depths placed at several different levels in the atmosphere over surfaces with a wide range of albedos. Duplication of such tables for a variety of effective particle sizes greatly increases the demand for computer memory and access time. To minimize the computer demands and allow for variable particle radiative properties, Minnis et al. (1993b) developed a reflectance parameterization that interpolates between values in lookup tables of cloud visible reflectance. Their parameterization is applicable over any low-albedo surface at any altitude. They also developed a simple parameterization to describe the effective emittance as a function of cloud particle distribution and viewing zenith angle. Although their model incorporated infrared scattering by cloud particles, it was not capable of computing effective emittances exceeding unity. Thus, clouds with moderate optical depths or thin clouds at higher viewing angles could not be properly characterized. Ou et al. (1993) developed a relatively simple parameterization of 3.73-μm emittance based on the 10.8-μm emittance for a hexagonal ice crystal size. However, the accuracy of that method is unknown .

A set of well-understood models that are spectrally consistent and complete is needed for simulating and interpreting cloud radiance fields. This paper addresses that need. Model calculations are performed to construct a set of lookup tables for visible (VIS) and solar-infrared (SI; 3.73- and 3.90-μm) reflectance for a wide range of particle sizes. Various interpolation techniques are tested to determine the best method for estimating reflectance between node points. Effective emittance is also computed for the same particle distributions using a range of realistic cloud and clear-sky temperatures for several wavelengths commonly used by operational meteorological satellite imagers. These emittances are parameterized using a simple polynomial function that yields more realistic and accurate radiances than previous models. Errors are estimated relative to the detailed radiative transfer calculations for both the reflectance and emittance models. Examples are given to demonstrate the utility of these models in satellite analyses and simulations.

2. Radiative transfer model and data

The adding-doubling (AD) radiative transfer models described by Minnis et al. (1993a) were used to compute reflectance and effective emittance for a variety of clouds at selected wavelengths. The spectra correspond to channels on current operational meteorological satellites. Refractive indices, m, of ice and liquid water used in the calculations were estimated for the AVHRR channels 3 (3.75 μm), 4 (10.7 μm), and 5 (11.9 μm) and for the GOES-8 Imager channels 2 (3.90 μm), 4 (10.8 μm), and 5 (12.0 μm) by convolving m_l from Hale and Querry (1973) and Warren (1984) with the filter functions for each channel. Channel 4 on both instruments is referred to as infrared (IR), while channel 5 is denoted as split window (WS). Mean filter functions were computed for the AVHRR channels using the values for NOAA-9, 10, 11, and 12. The GOES-Imager and AVHRR filter functions were obtained from Paul Menzel of NOAA (1994, personal communication) and from Kidwell (1991), respectively. These filter functions are shown in Fig. 1a for the VIS and wavelengths and in Fig. 1b for the IR and WS wavelengths. The index of refraction for wavelength λ = 0.65 μm was used for the GOES-7 visible and AVHRR and GOES-8 channel 1 because the real part of m varies slowly and the imaginary part is essentially zero for the wavelengths within those channels. The SI radiation sensed by a satellite may arise entirely from emission by the scene or it may also contain a reflected solar radiation component. At the longer SI wavelengths, the solar constant decreases with increasing wavelength (Iqbal, 1983), so that the spectral weighting of the filter function is influenced by the relative value of the solar constant. Thus, the weighting for the emitted component can differ from the solar component. Rather than using two different indices of refraction for each SI wavelength, a single value is computed by averaging m computed from the uniform- and solar-weighted filter-function convolutions. The resulting indices of refraction for each channel are listed in Table 1. Both the real and imaginary parts of m for ice at the WS wavelengths are greater than their IR counterparts suggesting less backscattered and more absorbed radiation for the IR channels. The difference between the WS and IR values of m_i(ice) is approximately double that for m_i(water). For the SI wavelengths, m_i(ice) is 100% greater than m_i(water).

a. Cloud microphysics and optical properties

The AD computations were performed for both cirrus and water-droplet clouds. The latter are represented by Mie scattering optical properties computed using the program of Wiscombe (1980) for effective radii, r_e = 2, 4, 6, 8, 12, 16, 32 μm based on the modified gamma distribution (Hansen and Travis, 1973) with an effective variance of 0.1.

Cirrus optical properties are based on the ray-tracing results of Takano and Liou (1989) for various combinations of randomly oriented hexagonal ice crystals having length-to-width ratios, L/D, of 20 μm/20μm (C20), 50 μm/40μm (C50), 120μm/60μm (C120), 300μm/100μm (C300), 750μm/160μm (C750). In addition, new ray-tracing results for very small ice crystals, 5μm/5μm (C5), 10μm/5μm (C10.5), and 10μm/10μm (C10), are also considered. The spheroidal parameterizations of Takano et al. (1992) were used to estimate some or all of the optical properties for smaller ice crystals at infrared wavelengths because their size parameters are well below the geometric optics limit. The single-scattering albedos, $\tilde{\omega}_0$, and extinction efficiencies Q were computed with the Takano et al. (1992) parameterizations at the IR and WS wavelngths for all of the ice crystals. Ray-tracing was used for C300 and C750 to derive the phase functions and asymmetry parameters, g, at these wavelengths. The spheroidal parameterization was used to compute g for the other sizes. The phase functions were then computed using the Heyney-Greenstein (HG) formula (Heyney and Greenstein, 1941). Because their aspect ratios are equal or close to unity, the average values for oblate and prolate spheroids having aspect ratios of v = 0.5 and 2.0, respectively, were used for C5, C10, C20, and C50. Except for values of Q, the ray-tracing results were used at the SI wavelengths for crystals C20 and larger. Solar-infrared single-scattering albedos were computed with the spheroidal approximations for crystals smaller than C50. The phase functions and subsequent values of g for these same crystals were determined by averaging the ray-tracing and parameterization-based HG phase functions. The directly transmitted component f_d arising from the ray-tracing calculations (Takano and Liou, 1989) was halved in these cases. For consistency, the Takano et al. (1992) spheroidal and large-crystal parameterizations were used to estimate Q for the visible channel. The other parameters for the VIS channel were taken from previous ray-tracing results at 0.55 μm (Takano and Liou, 1989). The 0.55-μm phase function and single-scattering albedo can be substituted for the VIS because the real indices of refraction at both wavelengths differ by less than 0.2% and their imaginary indices are insignificant (Warren, 1984).

The resulting single-crystal optical properties are given Tables 2, 3, and 4 for the VIS, SI, and IR channels, respectively. At the VIS wavelengths, Q decreases with increasing D_e, while g generally increases with D_e. The exceptionally large value of g for C10.5 results from the large aspect ratio (L/D = 2), demonstrating the impact of shape on the scattering patterns. Its value also deviates from the trend in g seen for the SI data. The peak in Q for C10.5, however, is due more to its size parameter ($\pi D_e / \lambda$) than to its shape. Because of the large size parameters, Q and g vary monotonically for the IR and WS wavelengths.

The single-scattering albedos, which are critical for particle size determination, are essentially monotonic with D_e for all of the considered spectra.

These optical properties were then integrated over a variety of ice crystal size distributions. A subset of the size distributions from Ou et al. (1993) are used here to provide a continuous series of increasing ice particle effective diameter,

$$D_e = \frac{\int_{L_1}^{L_2} D \cdot LDN(L)\, dL}{\int_{L_1}^{L_2} DLN(L)\, dL}, \qquad (1)$$

where N is the normalized number of particles per unit volume in a given size bin and L_1 and L_2 are the respective lengths of the smallest and largest crystals in a size distribution. Several additional distributions were developed to extend the size range from contrail-sized to very large effective crystals and to provide a smoother change of cloud properties with effective particle size. The physical characteristics, D_e , mean volume V, and cross-sectional area A of the resultant effective particles, for the integrated size distributions are given in Table 5. The size distributions include those for cold cirrus (CC), cirrostratus (CS), and cirrus uncinus (CU) given by Takano and Liou (1989) and a warm cirrostratus (WCS) distribution that is an average of the warm cirrus and CS distributions from Takano and Liou (1989). The NOV and OCT distributions refer to data taken Nov. 1 and Oct. 22, 1986 during the First International Satellite Cloud Climatology Regional Experiment (FIRE) First Cirrus Intensive Field Observation (Cirrus IFO-I). Distributions derived from the results of Heymsfield and Platt (1984) for cirrus at temperatures T = -40 and -60°C are designated T40 and T60, respectively. The T40, T60, NOV, and OCT distributions were discussed by Ou et al. (1993). A contrail cirrus (CON) distribution was developed from the data of Poellot and Henderson (1994) based on FIRE Cirrus IFO-II aircraft measurements taken in a contrail embedded within a cirrus cloud during a November 22, 1991 flight. Two other distributions were established to represent the extremes of the ice crystal sizes: a new contrail (NCON) comprising only particles smaller than C20 and a large-particle cirrus (LPC). These last three discrete distributions are given in Fig. 2. The C10.5 particles are included in the NCON distribution to make it more consistent with the other distributions which contain some crystals with significant aspect ratios.

Another key parameter is water path for liquid and ice in a cloud. Given the definitions for optical depth and liquid water path, it can be shown that the liquid water path is,

$$LWP = \frac{4\delta_{liq} r_e t}{3Q_{VIS}} \qquad (2)$$

for a given effective droplet radius and visible optical depth τ. No subscript is used for the visible optical depth because it will serve as the reference optical depth for all of the calculations. In (2), the liquid water density δ_{liq} = 1.0 g cm^{-3}. Similarly, using the discrete ice crystal distributions, the ice water path of the model cirrus clouds is

$$IWP = \frac{\delta_{ice} \sum (V_i N_{oi})\, \tau}{\sum Q_{VIS} A_i N_{oi}}, \qquad (3)$$

where N_{oi} is the normalized number of crystals per unit volume in given size bin i represented by a particular hexagonal crystal of size L/D. The density of ice δ_{ice} = 0.9 gcm^{-3}. A regression fit to the results of applying (3) to all of the distributions gives the following formula for ice water path in g m^{-2}:

$$W_{ice} = (2.66 + 0.134\, D_e + 2.41\text{x}10^{-3}\, D_e^2 - 7.26\text{x}10^{-6}\, D_e^3)\,\tau. \qquad (4)$$

This formulation yields an rms error of 6% over the applicable size range of D_e = 5 - 135 μm. It should not be applied outside of this range.

Figures 3a and 3b show the phase functions for a range of ice cloud models for λ = 0.65 and 3.75-μm, respectively. For both wavelengths, the largest particles have more forward and less side and backscattering than the smaller crystals. The scattering is nearly identical for scattering angles Θ > 30° for the smaller VIS models. The 22° and 46° halos seen in the VIS phase functions are replaced by a single halo at 30° for λ = 3.75 μm that nearly disappears for the NCON distribution. The location and magnitude of the halos are complicated function of crystal shape, orientation, and size parameter. Halos and other sharp features tend to diminish as the shape becomes more amorphous (e.g., Macke et al., 1996) and as the size parameter decreases. Thus, the SI ice crystal phase functions are generally much flatter than their VIS counterparts. The Mie scattering phase functions (Fig. 4) show a more complex variation with particle size for the two wavelengths. The visible Mie phase functions (Fig. 4a) are characterized by the extensive minimum at scattering angles, 80° < Θ < 130° and the rainbow maximum near Θ = 138°. Both features are more pronounced for the larger droplet size. The Mie scattering phase functions for 3.75 μm (Fig. 4b) generally have a less pronounced minimum in the side-scattering directions. The features tend to become smoothed as the size parameter decreases. Forward scattering increases with particle size for both wavelengths. Hansen and Travis (1974) provide a detailed discussion of Mie scattering.

The variations of the optical properties with effective particle size for all channels are listed in Tables 6, 7, and 8. The VIS values for $\tilde{\omega}_o$, are not listed in Table 7 because they are all essentially equal to unity (e.g., Table 2). The values for all three of the parameters vary smoothly with effective radius because of the functional form of the size distribution. In contrast, the discrete ice crystal distributions do not result in a completely monotonic variation of each property with effective diameter. A more monotonic change with D_e can be obtained by excluding CS and NOV from the parameterization. The single-scattering albedos for the IR and WS channels increase with increasing particle size while they decrease with increasing particle size for the VIS and SI wavelengths. At highly absorbing wavelengths, $\tilde{\omega}_o$, increases up to a limit of ~ 0.55 as a result of an increase in diffraction and other scattering with particle size. Diffraction removes energy available for absorption. Similarly, at the mildly absorbing SI wavelengths, $\tilde{\omega}_o$ (absorption) decreases (increases) as the volume of the particle grows, but is limited to ~0.54 primarily because of diffraction. The refracted component is initially large but decreases as the path length through the particle provides a greater probability for absorption.

Despite having larger values of m_i, the WS values of $\tilde{\omega}_o$, are greater than their IR counterparts for ice crystals. The WS values for water droplets are smaller than the corresponding IR values. The real part of the imaginary index of refraction can have a large impact on $\tilde{\omega}_o$. For example, replacing the 10.8-μm water-droplet m_r with the 11.9-μm value (1.258) of m_r doubles $\tilde{\omega}_o$ for small water droplets and significantly increases it for larger droplets. Because the external reflection of incident rays increases with m_r (Hansen and Travis, 1974), the opportunity for absorption decreases with increasing m_r. For water droplets, m_r(11.9 μm) < m_r(10.8μm) yielding the expected low single-scattering albedos for 11.9 μm. Thus, both parts of the index of refraction must be considered when using it to estimate the changes in single scattering albedo. The retrieval of particle size is based on the variation of all three parameters, especially $\tilde{\omega}_o$. Differences between the spectral values can be exploited to obtain additional information such as phase or optical depth.

b. Reflectance and emittance computations

The reflectance, ρ, at a particular set of solar zenith, viewing zenith, and relative azimuth angles, θ_o, θ, and ψ, respectively, is one parameter of interest for satellite retrievals of cloud properties. Thus, ρ was computed with the AD model for λ = 0.65 μm using 41 Gaussian quadrature points at ψ = 0, 5, 15, 30, 45, ..., 150, 165, 175, 180° for the optical depths τ = 0.25, 0.5, 1, 2, 3, 4, 8, 16, 32, 64, and 128. Linear interpolation was then used to construct a regular array of 11 zenith angles using μ_o = 1.0, 0.95, 0.85, ..., 0.05 and μ = 1.0, 0.9, 0.8, ..., 0.1, where $\mu_o = \cos\theta_o$ and $\mu = \cos\theta$. Reflectances were computed in a similar fashion at λ = 3.75 and 3.90 μm, but only for $\tau \leq 32$, because ρ is essentially constant at greater optical depths for most particle sizes. The interpolated, computed reflectances were compiled in lookup tables that require approximately 0.25 and 0.15 megabytes of computer storage per particle size for the VIS and SI channels, respectively. The directional albedo, $\alpha(\mu_o)$, and spherical or diffuse albedo, α_d, were also calculated by integrating ρ over the viewing angles and $\alpha(\mu_o)$ over the solar zenith angles, respectively. In this parameterization, the VIS optical depth serves as the reference optical thickness. The optical depth for a given wavelength is related to the visible optical depth by

$$\tau_\lambda = \frac{\tau_{vis} Q_\lambda}{Q_{VIS}}. \qquad (5)$$

Spectral effective emittance, $\varepsilon(\lambda)$, was determined by using the AD model to compute upwelling radiances, $B_\lambda(T)$ for $0° \leq \theta < 72°$, where B is the Planck function. The computations were performed for surface temperatures T_g = 240, 260, 280, 300, 320K; water-cloud temperatures T_C = 240, 255, 265, ..., 295K; and ice-cloud temperatures T_C = 195, 210,..., 270K. The radiances were computed for spectral optical depths corresponding to the VIS optical depths τ = 0.25, 0.5, 1, 2, 3, 4, 8, 16, and 32 using (5) to convert from τ to τ_λ. In the calculations, it was assumed that the surface is black and all atmospheric moisture is confined to the sub-cloud layer. This assumption produces a negligible error in application because surface albedos are small at these wavelengths. Thus, any multiple scattering between the cloud and surface will yield upwelling radiances that are much smaller than the surface-emitted radiance. The model is formulated in terms of the upwelling radiation at cloud base whether it emanates from the atmosphere, the surface, or a combination of the two. A nominal atmospheric optical depth was determined based on the layer temperature and the wavelength using a relatively moist atmosphere. Several cases were also evaluated using totally dry atmospheric layers. Clear-sky equivalent blackbody temperatures, T_S, were computed for each channel using the specified atmospheric optical depths and effective atmospheric temperatures. The air temperature closest to the average of T_C and T_g and the corresponding optical depth were used to represent the subcloud layer for a given case. The effective emittance for channel i is

$$\varepsilon_i = [B_i(T) - B_i(T_S)] / [B_i(T_C) - B_i(T_S)]. \qquad (6)$$

This quantity includes the effects of multiple scattering and absorption by the cloud layer. In application, attenuation by any moisture above the cloud layer can be taken into account if the temperature and humidity profiles are known. At the SI channels, where surface reflectance is higher than at the IR and WS wavelengths and downwelling solar radiation can be significant, the contribution of surface-reflected solar radiation must be added to the upwelling surface-emitted radiance explicitly.

In the absence of scattering, the absorption emittance is simply

$$\varepsilon_{ai} = 1 - \exp[- (1 - \tilde{\omega}_{oi})\ \tau_i\ /\ \mu]. \qquad (7)$$

Absorption emittance is the quantity that is typically used in most satellite cloud parameter retrievals or simulations. Differences between ε and ε_a depend mostly on $\tilde{\omega}_o$.

3. Results and analysis

a. Reflectance

For comparison, the reflectances were normalized to yield anisotropic factors,

$$\chi(\mu_o,\mu,\psi) = \frac{\rho(\mu_o,\mu,\psi)}{\alpha(\mu_o)}.$$

Examples of these anisotropic reflectance factors are shown in Figs. 5 and 6 at $\mu_o = 0.65$ and $\tau = 1$ for r_e = 6 and 16 μm and for T60 and OCT for λ = 0.65 and 3.75-μm, respectively. Similarities in the reflectance patterns of different particle sizes for ice at a given wavelength follow from the commonalities in the phase functions (Fig. 3). Variations in the 0.65-μm reflectance patterns for the water droplets (Figs. 5c-d) arise from phase function differences. For example, the rainbow peak at $\Theta = 138°$ is more pronounced for larger droplets while the backscatter maximum is diminished (Fig. 4a). At $r_e = 16$ μm, a relative reflectance maximum appears at $\theta = 65°$, $\psi = 135°$ in Fig. 5d, but not at $\theta = 53°$, $\psi = 180°$, where a distinctive maximum occurs for r_e = 6 μm (Fig. 5c). Even more striking reflectance differences between the two sizes are conspicuous at 3.75 μm. The differences between the droplet and ice crystal VIS reflectance patterns are also significant and have been noted in previous studies (e.g., Minnis et al., 1993a). Discrepancies between the ice and water reflectances are also quite noticeable in the SI reflectance patterns (Fig. 6) although there are substantial differences between SI and VIS reflectance patterns for the same effective particle size.

Integration of the bidirectional reflectances yields the albedos. Figures 7 and 8 show examples of albedo as a function of μ_o for the models in Figs. 5 and 6, respectively, at various optical depths. The small-particle albedos are typically greater than those for the larger particles of both phases. Water droplets reflect more than the ice crystals at 3.75 μm because of the larger values of $\tilde{\omega}_o$ for liquid water. Conversely, the ice crystals typically produce greater albedos than the water droplets at 0.65 μm because g is generally smaller for the crystalline shape than for the spheres. Albedos at 0.65 μm exceed those at 3.75 μm because of the latter's smaller values of $\tilde{\omega}_o$. At smaller optical depths, the relative increase of SI albedo with decreasing μ_o is less than the corresponding increase in the VIS albedo.

The phase and particle size dependencies are more evident in the variations of diffuse albedo with optical depth shown in Figs. 9 and 10 for 0.65 and 3.75 μm, respectively. Except for r_e = 2 μm, the diffuse VIS albedo (Fig. 9) for a water droplet cloud at a given optical depth is less than that for most ice clouds. At r_e = 2 μm, α_d is similar to that of a cloud composed of medium sized ice crystals (T40). Conversely, most of the ice-cloud SI albedos (Fig. 10b) are less than the water droplet clouds (Fig. 10a) at a given SI optical depth. Exceptions are the contrail distributions which produce albedos comparable to the 6- and 12-μm water droplets. More typical cirrus clouds have SI albedos that are less than those for r_e = 16 μm. There is overlap between the diffuse albedos for droplets smaller than 8 μm for $\tau_{3.75} < 3$ ($\tau < 4$). This overlap results in the well-known non-monotonic variation of reflectance with droplet size that makes the retrieval of r_e ambiguous for methods using the SI data (e.g. Han et al., 1994). It results from the location of the extinction efficiency peak near r_e = 4 μm (Table 8). At larger optical depths, the albedo overlap disappears because increasing absorption due to the monotonically decreasing values of $\tilde{\omega}_o$ offsets the peak scattering and extinction efficiencies.

b. Emittance

The effective emittances for all of the AVHRR channel-3 and 4 calculations at r_e = 6 μm are shown in Figs. 11a and 11b, respectively, as functions of $\log(\tau/\mu)$. There is considerable variability in these results, especially for channel 3 as a result of increased scattering. There are many points having $\varepsilon > 1$. This effect, in most cases, is confined to large optical depths, large viewing zenith angles, and low contrast between the cloud and the surface. Fits to the model given by Minnis et al. (1993a),

$$\varepsilon = 1 - \exp[\ a\ (\tau / \mu)^b\ ], \qquad (8)$$

where a and b are regression coefficients, using only data with $\varepsilon < 1$ are also shown for comparison with the data. Although many of the data points fall on the

curve, there are a substantial number that do not follow this simple relationship. It is obvious that the simple functions traditionally used to fit the data (e.g, Minnis et al. 1993b) cannot include all of the points, in particular those having $\varepsilon > 1$.

To examine the variability not explained by τ/μ, the emittances are replotted in Fig. 12 as functions of the temperature difference, $\Delta T_{SC} = T_S - T_C$. The channel-3 effective emittances (Fig. 12a) have maximum values of ~2.9, while the IR emittances (Fig. 12b) peak at ~1.7. Greater scattering at 3.75 μm gives rise to the larger effective emittances. Effective emittance increases with decreasing ΔT_{SC}, in an almost logarithmic fashion, especially for channel 3. The horizontal spread in a given string of points is due to the change in μ. For the dry atmospheres, there is no horizontal spread, so the strings form vertical lines at particular differences (e.g., ΔT_{SC} = 30 K in Fig. 12a). For the largest values of ΔT_{SC}, ε <1 for optical depths as large as 16 or 8 at 3.75 (Fig. 12a) and 10.8 μm (Fig. 12b), respectively. Because of this apparent logarithmic dependence, values of $\Delta T_{SC} < 4$ K were not used in the parameterization. As shown later, large emittance errors for low thermal contrast have minimal impact on the derived temperature.

Regression analyses using clear-cloud radiance differences, ΔT_{SC}, T_S, T_C, τ, and μ revealed that functions of T_S, ΔT_{SC}, τ, and μ were most highly correlated with ε for a given particle size. For example, for r_e = 6 μm at λ = 3.75 μm, the linear correlation coeffcients for ε with T_C, $1/\ln(T_S)$, $1/\ln(\Delta T_{SC})$, τ, and μ are -0.14, 0.49, 0.60, and -0.21, respectively. When T_S and ΔT_{SC} are included together in a multiple regression, T_C becomes an insignificant variable in the regression. Except for τ, the correlations decrease with increasing r_e. Han (1992) also found significant dependence of the 3.75-μm emittance on surface and cloud temperatures. At 10.8 μm, the respective coefficients are 0.06, -0.05, 0.13, 0.66, and -0.26. To account for these dependencies and minimize the errors, multiple regression was performed for each of the nine discrete values of τ using the formula,

$$\varepsilon(\zeta,\mu,\xi) = \sum_{i=0}^{2}\sum_{j=0}^{4}\sum_{k=0}^{1} d_{ijk}\zeta^i\mu^j\xi^k, \qquad (9)$$

where $\zeta = 1/\ln(\Delta T_{sc})$ and $\xi = 1/\ln(T_s)$. The coefficients, d_{ijk}, were determined by minimizing the squared error. These regression analyses generated nine sets of 32 coefficients for each microphysical model and spectral band. Emittances for optical depths off the nodes are determined by 4-point Lagrangian interpolation in $\ln\tau$ for all interior values and linear interpolation for $\tau < 0.25$ and $\tau > 16$. If $\tau > 32$, $\varepsilon = \varepsilon(\tau=32)$. To further reduce errors, Lagrangian interpolation is used for $16 < \tau < 32$ if the difference in ε between optical depths of 16 and 32 is greater than 1%. For a given set of conditions, ε is found with the parameterization which consists of (9) and the interpolation system. A four-parameter regression fit using an additional polynomial in $\ln\tau$ was also examined, but it did not produce a sufficiently accurate fit for the SI wavelengths.

The rms or standard errors of the estimates (SEE) for the regression fit to (8) shown in Fig. 11a for the 6-μm water droplets at 3.75 μm are 0.363 and 0.140 for all of the data and for $\varepsilon < 1$, respectively. The corresponding errors are reduced to 0.014 and 0.012 with (9). For the 10.8-μm curve in Fig. 11b, the respective SEEs are 0.084 and 0.049 compared to 0.002 and 0.002 for the fit to (9). Values for SEE in absolute emittance are plotted for all of the liquid and ice particle models in Fig. 13 for channels 3, 4, and 5. The results for the corresponding GOES-8 spectra are not shown because they are nearly identical to those for the AVHRR channels. The greatest SEE's occur for the small particles at SI wavelengths where $\tilde{\omega}_o$ is large. Scattering complicates the representation of effective emittance. The SEE's for the longer wavelength channels are considerably smaller than those for the SI channels and the ice SEE's are substantially less than those for the water droplet models. The new parameterization not only accounts for $\varepsilon > 1$, it substantially improves the emittance estimates for $\varepsilon < 1$ for both wavelengths.

An effective technique for demonstrating the variability of emittances is to plot the brightness temperature difference, $BTD_\lambda = T_\lambda - T_{IR}$ or $T_{IR} - T_\lambda$, as a function of the IR temperature T_{IR}. Figure 14 shows the *BTD*s computed using the 3.75 and 11.9-μm parameterizations for a range of r_e and D_e at $\theta = 30°$, T_g = 295K, and T_C = 260K for $\tau \le 16$. The water-droplet BTDs cover a greater range at a given value of T_{IR} than the corresponding ice-crystal values for both wavelengths. Thus, there is more sensitivity in the BTDs to changes in droplet size than to variations in ice crystal size. At 11.9 μm (Figs. 14c-d), the BTD increases with decreasing particle size for both phases. Similar behavior is evident for most of the SI ice-crystal distributions (Fig. 14b). Conversely, most of the SI water-droplet BTDs (Fig. 14a) increase with increasing effective radius. Both phases have a non-monotonic variation in BTD at 3.75 μm with the maximum BTDs occurring at $r_e \approx 16$ μm and $D_e \approx 24$ μm. At greater clear-cloud temperature contrasts, the ice-crystal BTD maximum shifts to smaller sizes. Thus, at colder cloud temperatures, it is possible to obtain a monotonic range in D_e from 18 to 135 μm. The BTDs are less than or equal to zero for τ = 16 for all of the models except for r_e = 2 and 4 μm at the IR and WS wavelengths. Because of the extremely small extinction efficiencies at these wavelengths, the emittances are less than unity at

$\tau = 16$. Thus, the 10.8 and 11.9-μm temperatures do not reach T_c for $r_e = 2$ μm.

Given only SI and IR data, it would be difficult to unambiguously determine particle size when r_e exceeds ~10 μm or when $D_e < 50$ μm in the case of Fig. 14. Because the particle sizes corresponding to the maximum BTDs vary somewhat with ΔT_{sc}, the range of potentially ambiguous particle sizes will also vary with ΔT_{sc}. The monotonic changes in Figs. 14c and 14d may be used together with the SI BTDs, however, to resolve both phase and particle size in this particular case. This non-monotonic behavior may explain why contrails are only occasionally detectable with the SI data, but are often seen in images of BTDs from 10.8 and 11.9 μm data (e.g., Lee, 1989). The overlap of the contrail-sized-particle BTDs with those for larger ice crystals should often make contrails indistinct from other cirrus clouds at the SI wavelengths at night. The addition of the significant solar reflection from small-particle contrails (e.g., Fig. 10) would render the contrails more distinguishable in certain conditions during the daytime. At 11.9 μm, small-particle contrails should be more easily identified because of the monotonic variation of BTD with D_e.

c. Daytime solar infrared

During the daytime, the solar and thermal components at SI wavelengths must be combined to obtain the radiances for these wavelengths. Neglecting atmospheric effects, the total radiance for the SI may be approximated as

$$B_\lambda(T_\lambda) = \varepsilon_\lambda B(T_c) + (1 - \varepsilon_\lambda) B(T_b) + \rho_\lambda \mu_o E_\lambda \delta(d), \qquad (10)$$

where T_b is the equivalent blackbody temperature of the total upwelling radiance below the cloud, E_λ is the spectral solar constant, δ is the normalized Earth-sun distance, and d is the day of the year. In the absence of atmospheric absorption, the upwelling radiance below the cloud is approximated as

$$B(T_b) = \varepsilon_{g\lambda} B(T_g) + \alpha_{g\lambda} \{E_\lambda \mu_o [1 - \alpha_\lambda(\mu_o) - \varepsilon_\lambda (\mu_o)]\}, \qquad (11)$$

where ε_g is the surface emittance, α_g is the surface albedo, α_λ is the cloud albedo, ε_a is the spectral absorption emittance, and T_g is the skin temperature of the surface. At night or when $\alpha_{g\lambda} = 0$, the first term in (11) is equivalent to $B(T_s)$ and $B(T_b) = B(T_s)$. At night, therefore, (10) reduces to (6). In (11), the first term in the brackets is the solar radiation reaching the surface; it is assumed to be diffuse. Because the reflected component is removed explicitly with the cloud albedo, the absorption emittance is used in this term. Secondary and higher-order reflections between the cloud and the surface are neglected in this approximation.

4. Discussion and applications

a. VIS reflectance interpolations

Application of the reflectance models to specific angles and optical depths requires interpolation between the lookup table values. Various interpolation methods were evaluated using the VIS reflectances calculated for a variety of angles and optical depths different from those used to create the lookup tables for the model. AD calculations were performed for the CS and 8-μm water droplet models using random sets of viewing and illumination angles selected for $\mu_o > 0.15$, $\mu > 0.34$, and $0 \le \psi \le 180°$. Ten randomly selected values of $\log\tau$, where $\log\tau = -1, 2$, were used to complete the calculations resulting in a total of 12,250 samples for each model. The interpolations for the CS and 8-μm droplets should be representative for the ice and water droplet models.

Reflectances were estimated from the lookup tables using nearest-node values and interpolations with various combinations of linear and Lagrangian methods. The results were compared to the AD values to determine the optimal technique. Table 9 summarizes the errors in estimated reflectance for a few of the techniques. The hybrid interpolation combines linear interpolation in ψ and $\ln\tau$ with 4-point Lagrangian interpolation in μ_o and μ. The hybrid method is comparable to the 4-dimensional, 4-point Lagrangian technique and is more accurate than linear interpolation which is actually log-linear in τ for $\tau > 0.25$. Overall, the bias errors are -0.5 and 0.1% for the 8-μm and WCS models, respectively. The corresponding rms errors are 3.0 and 9.9% compared to 21.8 and 19.0% for the nearest node approach. Although the hybrid method is more accurate than the linear technique, it is computationally slower by a factor of 2. Thus, the accuracy of the linear method may be sufficient for a particular application. There appears to be no reason for using more computationally expensive 4-point Lagrangian method instead of the hybrid technique.

To better understand the estimated reflectance errors, the means and extremes from the hybrid interpolation are plotted as a function of scattering angle in Fig. 15. For the 8-μm model (Fig. 15a), the mean errors are greatest near 138° and 179° and minimal elsewhere. These error variations depend on the features of the phase function. The change in the phase function with Θ between 120° and 140° is greater than an order of magnitude for $r_e = 8$ μm (e.g., Fig. 4a) and is highly nonlinear. Similarly, the phase function increases by a factor of 8 between 174° and 180°. Thus, interpolation between the relatively low resolution of the model nodes is insufficient to capture the shape of the curve at these important angles. The dependence of error on the phase

functions is seen more clearly in the CS results (Fig. 15b), where the features of the CS phase function (similar to WCS in Fig. 3a) are mimicked in the mean reflectance errors. Here the greatest errors occur in the forward ($\Theta < 50°$) and backscattering ($\Theta > 174°$) directions. Except for the cross-scattering directions (60 - 105°) in the CS model, the error extrema in Fig. 15 differ substantially from the means. Most of the errors are considerably smaller than the extrema. The largest relative differences primarily occur for very small optical depths where single-scattering dominates.

These errors may be reduced by including more nodal points or by saving the Fourier coefficients from the azimuthal expansions used in the AD calculations instead of retaining single values at a given ψ. However, the zenith variations affecting the scattering angle could still cause large uncertainties if the number of nodes remained small. The size and complexity of the lookup tables must be weighed against memory and processing time constraints. Capturing all of the phase function features accurately in a lookup table will still be elusive, however, because of the various combinations of μ_o, μ, and ψ that can determine Θ. Due to generally smoother phase functions at 3.75 μm (Figs. 3b and 4b), the reflectance interpolation errors will be smaller except when $\Theta > 174°$ for the ice models and when $\Theta > 135°$ for the 32-μm water droplet model.

Although these models may be used for a variety of applications, they will most often be applied to satellite observations. In practice, the overall interpolation errors may be better or worse depending on the particular viewing geometry of a given satellite. As shown in the Appendix, bias and rms errors due to interpolation are smaller than the values in Table 9 for more than half and 75%, respectively, of the considered realistic satellite sampling scenarios.

b. Cloud water path and albedo

The VIS albedo varies by a maximum of ~0.1 for a particular optical depth (Fig. 9) over the range of particle sizes considered here. The variation of α_d with r_e for a fixed value of τ is much less than that for a fixed value of cloud water path. Ackerman and Stephens (1987), Stephens and Greenwald (1991), and others have shown both theoretically and empirically that the broadband solar albedo can change dramatically with r_e for a fixed value of LWP. It is instructive, however, to understand the importance of particle size when relating the hydrological cycle to the VIS albedo or, consequently, the VIS radiance field. This relationship depends on how the albedo changes when a particular amount of water vapor is condensed or frozen in the atmosphere giving rise to a fixed liquid or ice water path.

Figure 16 demonstrates the sensitivity of the VIS albedo to particle size in terms of water path. The albedo can change by more than 0.70 for a given amount of liquid or ice water depending on the particle size distribution assumed in the calculation. For liquid water clouds (Fig. 16a), the albedo range for constant LWP exceeds 0.2 for LWP between 2 and 600 gm^{-2}. The same range in albedo occurs for IWP between 0.8 and 150. These wide ranges in albedo for a given cloud water path have serious implications for climate model calculations and for satellite-based retrievals of optical depth. For example, if a model calculation specifies LWP = 100 gm^{-2}, the VIS albedo can vary by 0.33 to 0.92 for effective droplet sizes between 32 and 2 μm, respectively. An assumption of r_e =10 μm, for instance, converts the LWP to $a_d \approx 0.64$. For the frequently observed effective droplet sizes between 4 and 16 μm, this assumption could lead to albedo errors as great as 0.16. Conversely, the optical depth retrieved using the 10-μm water droplet assumption can often lead to errors in τ or LWP of more than 100% for commonly observed droplet sizes. Similar errors can also occur for cirrus clouds.

c. Emittance and temperature errors

Minnis et al. (1993b) showed that (8) provides a more accurate representation of ε than (7). As demonstrated earlier, (9) decreases the uncertainties in ε estimated with (8) by a additional 100% or more. Thus, the errors from the earlier models are considerably greater than those for the present parameterization. Although computationally more intensive, the current technique provides more accuracy and operates over a greater range of optical depths than the earlier approaches to effective emittance. The simpler methods represented by (7) and (8) may be sufficiently accurate for the IR and WS bands in some applications. As the precision of remote sensing measurements increases, however, the higher accuracy of (9) will be required even for the less sensitive infrared window bands.

Effective emittance primarily serves as an intermediate parameter in remote sensing. The simulation of the radiance $R = B_\lambda(T)$ or equivalent blackbody temperature T_λ at the top of the atmosphere is ultimately the quantity of interest. Thus, it is necessary to consider the sensitivity of T to errors in ε. Given the definition of T in (6) and the Planck function, it can shown that errors in T due to the emittance errors can be estimated by

$$\Delta T \approx T\left(\frac{\Delta\varepsilon}{\varepsilon}\right)S_{T|\varepsilon}. \qquad (12)$$

where the sensitivity of the temperature calculation to errors in the emittance estimate is

$$S_{T_\lambda|\varepsilon} = \varepsilon T_\lambda \left(\frac{\Delta R}{R_\lambda} \right) \left(\frac{\lambda}{c_2} \right) \left[\frac{1}{1 + \lambda^5 R_\lambda / c_1} \right], \quad (13)$$

and $\Delta R = B\lambda(T_C) - B_I(T_S)$. From (13), it is expected that if the emittance is small or T_C is close to T_S, then $S_{T_\lambda|\varepsilon}$ will be small. Consequently, the temperature error will also be small. Conversely, if both ε and ΔT_{SC} (i.e., ΔR) are large, then a minimal emittance error can cause a large temperature error.

Values of ΔT were computed as the differences between the original AD and the corresponding parameterized temperatures for r_e = 8 μm and T40. More than 88 and 95% the differences are less than ± 0.5K for water droplets and ice crystals, respectively. Although they may be as large as -10K occur in a few instances, errors less than ± 1K occur in 95% of the water droplet cases. The rms errors for all of the models are summarized in Table 10 for the two SI wavelengths. When $\varepsilon < 1$, the errors are considerably smaller than for all cases indicating that the characterization of effective emittances greater than unity is difficult, even with the current approach

The temperature errors are generally greatest for smaller particle sizes (Table 10). The errors are largest for the NCON distribution and decrease by a factor of two as particle size increases to the CC distribution. Except for contrail distributions, the water-droplet ΔT's are similar to the ice-crystal temperature errors. Because of the greater possible range in ΔT_{SC}, the sensitivity factors can be much greater for the ice-crystal than for the water-droplet models. Thus, ΔT for the ice models can be larger than that for the liquid models despite the greater emittance errors for the water droplets. In all cases, ΔT increases with τ (or ε) and ΔT_{SC}, as expected from (12) and (13). For channels 4 and 5, the temperature errors have negligible size dependence and no significant differences between all ε and $\varepsilon < 1$. At both IR and WS wavelengths, the rms temperature errors for water droplets and ice are ~ 0.06 and 0.04 K, respectively.

The parameterizations given by (9), (11), and the interpolation technique were tested by comparing AD calculations that explicitly included both the solar and emitted SI components for an independent dataset (see Appendix). For nocturnal cases, the errors in simulated values of T_{SI} which would be observed by a satellite are approximately ± 0.5 and 1.0K for water-droplet and ice-crystal clouds, respectively. The latter error reduces to 0.6K if temperature and emittance interpolations in optical depth are used for $\tau > 8$ and $\tau < 8$, respectively. During the daytime, the rms errors are approximately ± 0.6 and 1.0K, respectively, for water and ice if the optimal interpolations are used. The temperature errors can be as great as 10K for some scattering angles and large cloud-surface temperature contrasts. The use of (11) in the parameterization of combined cloud and surface radiation introduces no significant errors in the simulated temepratures.

d. Applications

The models and parameterizations developed here can be used in either simulations of radiance fields for specified cloud conditions or in the retrieval of cloud properties from multispectral radiances. Examples of the simulations were given in Fig. 14. Figures 17-20 show the AVHRR imagery and the results of the parameterization calculations plotted over two-dimensional histograms of the AVHRR BTDs. Data from the NOAA-11 AVHRR are given in Fig. 17 for cirrus clouds over the Coral Sea east of Australia observed January 17, 1993. The VIS-IR histogram (Fig. 17b) is analyzed with the layer bispectral threshold method (LBTM; see Minnis et al., 1995) which divides the histogram into clear (box at dark, warm corner) and cloudy regions (remaining area). The three curves define the relationships between VIS counts, which are directly proportional to reflectance, and T_{IR} for clouds at the tropopause (gray, steepest line), 6 km (middle line), and 2 km (nearly horizontal line extending rightward from VIS count of 14). The 2-km line is defined using r_e = 10 μm, while the other two are computed using the CS model. These lines would continue off the graph gradually becoming horizontal at the temperature for their particular altitudes (see Minnis et al., 1993b). The numbers on the plot indicate the frequencies of each pair of VIS count and T_{IR}. The LBTM analysis yields a high cloud with a center near 12 km with T_C = 237K. Using the LBTM result, the modeled SI BTDs for ice particle sizes between 24 and 45 μm plotted in Fig. 17c encompass most of the data suggesting an average value of D_e = 30 μm. The WS BTDs for the same particle sizes also account for most of the data in Fig. 17d indicating that the parameterizations provide a consistent spectral characterization of the observations.

Figure 18 shows the results for a low-level cloud observed in Fig. 17a from the NOAA-11 AVHRR. The structure of the VIS-IR histogram (Fig. 17a) and the LBTM analysis yield a midlevel cloud deck at 3 km where T_C = 283.7 K. Using this result with a correction for water vapor absorption based on the correlated k-distribution technique (Kratz, 1995) to compute BTDs yields the curves for r_e = 8 - 16 μm that envelope most of the SI BTD data in Fig. 18b and some of the WS BTD values in Fig. 18c. The WS models do not account for all of the differences in optically thick cloud cases. The variation of T_{IR} for $BTD \leq 0$ K in Fig. 18c suggests that the cloud-top temperature actually varies from 282.5 to 285K so that no single curve can account for all of the data.

NOAA-14 IR data are shown in Fig. 19a for a multilevel case seen over the Gulf Stream east of Cape

Hatteras, North Carolina during January 16, 1997. A low-cloud layer is evident near 281K (1.1 km) in the corresponding VIS-IR histogram in Fig. 19b. Higher clouds do not appear to form a distinct layer in the VIS-IR data. However, the WS BTD data in Fig. 19d suggest an upper-level cloud between 252 and 262K. The closest sounding, taken from Wallops Island, Virginia, indicates a very moist layer under an inversion at 256K. Curves outlining much of the data can be constructed if it is assumed that there are two layers with T_{c1} = 281K and T_{c2} = 256K over a clear-sky temperature of T_s = 292K. Unlike a simple theoretical system, real multilayered clouds can present a very complex radiance picture. The curves overlaying the data in Figs. 19c and 19d represent only one scenario for this case. Curves A and B represent the BTDs for r_e = 8 and 12 μm, respectively, for the low cloud. These models, which account for many of the warmer data points, result in a spread of *BTD*(SI-IR) ~ 10K for the lower cloud at 281K. Although the corresponding curves in Fig. 19d do not appear to envelope many of the warmer data, the actual number of points within the curves is far greater than indicated by the discrete representation of the data. Furthermore, inclusion of the ~1.5K spread in the clear-sky *BTD*(IR-WS) in these curves would encompass many more of the warmer data.

The upper-level cloud in Figs. 19c and 19d is represented with a single particle size, T60 or D_e = 30 μm to illustrate the effects of a varying background. The value of T60 was selected because its curve (not shown), determined using T_{c2} over the clear background, bisected much of the colder data. Curves C and D in Fig. 19c were computed using the background radiances derived for an optically thin, low cloud yielding T_s = 285K and for the optically thick cloud at T_s = 281K, respectively. The maximum *BTD*(SI-IR) at 285K is ~ 18K and the minimum at 281K is ~10K. These differences were used to estimate the clear-sky reflectance for use in (11). The results apparently account for much of the colder data. Using these two background temperatures in the calculations for *BTD*(IR-WS) in Fig. 19d provides a consistent scenario; a large portion of the colder data points are encompassed by C and D. The T60 curve for a clear background (dotted line in Fig. 19d) accounts for some of the larger BTDs. The outlying colder points with smaller *BTD*(IR-WS) and larger *BTD*(SI-IR) probably correspond to optically thicker clouds at temperatures different from 256K. The remaining unexplained points are warmer than 275K with BTDs greater than explained by the water droplet models. These points may correspond to an optically thin high cloud near 220K. The cloud mass to the east in Fig. 19a contains many pixels with T < 225K. The Wallops sounding also indicates a very moist layer between 205K (11.5 km) and 226K (8 km). Except for the few outlying points, the parameterization results used here yield a consistent depiction of the observed data.

Further north during September 26, 1996, contrails were prevalent over Virginia, the Chesapeake Bay, and the adjacent waters of the Atlantic. Figure 20a shows some of these contrails in a NOAA-12 AVHRR IR image. The VIS-IR LBTM analysis (Fig. 20b) places these contrail clouds just below the tropopause at 11.4 km (T_c = 218K). For this cloud temperature, both the SI (Fig. 20c) and WS (Fig. 20d) BTDs indicate that the mean particle size is ~ 21 μm. This particle size is only slightly greater than the CON model developed to represent an old contrail confirming, at least in this case. the smaller size of ice crystals in relatively new contrails.

The final example seen in Fig. 21a is for a cirrus cloud observed in 4-km GOES-8 data taken at night over the north central Oklahoma Atmospheric Radiation Measurement (ARM) Program Central Facility (Stokes and Schwartz, 1994) during April 15, 1995. The ARM micropulse lidar returns (J. D. Spinhirne, 1995 personal communication, URL http://virl.gsfc.nasa.gov/mpl.html) indicate that the cloud center was located at 10.5 km or 230K. Model calculations were performed using T_c = 230K and the observed clear-sky temperature. Figure 21b shows the best-fitting model results plotted over the SI BTDs for data over the lidar site. Both the ice-crystal models, CC and WCS, and the water-droplet models, 2 and 4 μm, encompass most of the data. The water-droplet models, however, cannot explain the WS BTDs (Fig. 21c) which are also enveloped by the CC and WCS models. This consistency demonstrates the potential utility for using the WS data for phase selection.

These examples cannot fully represent the myriad of cloud conditions found in nature. Nor should it be concluded that the models can be used to accurately portray the radiances for any and all cloud systems. However, they demonstrate that the parameterizations can provide a realistic and spectrally consistent characterization of a variety of clouds in different viewing and illumination situations. Figures 17-21 show the models plotted over the data, but do not provide an objective retrieval of the cloud properties. The development of a methodology to retrieve phase, particle size, and optical depth is a complex process and beyond the scope of this study. The excellent agreement between the models and the data in these examples, though, show that the parameterizations derived here can be used in any retrieval method utilizing the AVHRR and GOES imager data.

e. Other considerations

The models developed here are based on a highly idealized set of cloud conditions and cannot be assumed to represent all clouds. Because infinite, plane-parallel clouds are used in the model calculations, it is likely that there are many situations, such as those involving broken, scattered, or horizontally inhomogeneous

clouds, in which these model results will not be applicable. Vertical cloud inhomogeneities in cloud particle size may also yield different radiances than those predicted from the parameterizations. Cloud ice particles can take a variety of shapes or orientations that may differ from the randomly oriented, hexagonal ice columns used here. The reflected radiance fields vary with changes in the ice particle orientation or shape changes (e.g., Takano and Liou, 1989; Macke et al., 1996). The dramatic effect of particle shape on g was demonstrated earlier in the discussion about the C10.5 crystal. Given the phase function and other optical properties, the calculations performed here can be applied to any particle shape, size, or orientation. Hexagonal columns were used here because they are relatively common in cirrus clouds (e.g., Heymsfield and Platt, 1984) and can occur as components in more complex ice crystals. Whether they are the best shape to characterize cirrus in general is an open question. Much more data analysis is required before it can be determined how accurately the present models represent actual cirrus. Future remote sensing techniques that determine both particle shape and size, however, would obviate the need for using a single shape in the cloud retrieval process. Conversely, additional knowledge of the distribution of ice particle shapes and sizes would permit more accurate simulations of the cirrus cloud radiance fields.

5. Concluding remarks

Global retrievals of cloud properties require an accurate, spectrally consistent, and computationally efficient representation of cloud radiances for all relevant viewing and illumination conditions observed from satellites. To address this need, parameterizations of reflectance and emittance for wavelengths commonly used for cloud property retrievals were developed and comprehensively evaluated in this paper.

The reflectance parameterization consists of a set of lookup tables covering a broad range of water-droplet effective radii and hexagonal ice crystal distributions for the visible and solar infrared channels on AVHRR and GOES. Values between the angle and optical depth nodes for a given particle size and optical depth can be most accurately and efficiently determined through a 4-point Lagrangian interpolation in the cosines of solar and viewing zenith angles and linear in relative azimuth angle and the natural logarithm of optical depth. Heretofore, the errors in reflectance due to interpolation have not been quantified. For the best interpolation method used here, the interpolation errors for the VIS models are generally less than or equal to 3% and 5% for water droplets and ice crystals, respectively, for useful satellite viewing conditions. For solar-infrared reflectance, the interpolation errors are less than 3% and 2% for droplets and ice crystals, respectively. The errors are greatest near the backscattering direction. In most conditions, however, the reflectance errors are minimal for both the visible and solar infrared wavelengths. Techniques for improving the interpolations were discussed.

The effective emittance for the solar-infrared and infrared-window wavelengths was parameterized with a multivariate polynomial in the cosine of viewing zenith angle, the clear-cloud temperature difference, and the surface temperature. The optical-depth dependence of effective emittance, which includes both the scattering and emission effects for a particular cloud particle size, is most accurately determined through 4-point Lagrangian interpolation between optical depth nodes. Overall, the effective emittances for the infrared window and split window computed with the more exact adding-doubling radiative transfer model can be reproduced to within $\pm$ 0.4% using the current parameterization. The corresponding effective emittances for the solar infrared channels are generally within $\pm$ 2% and $\pm$ 1% of the adding doubling results. These new parameterizations yield an order of magnitude improvement over previous models. In addition, they account, for the first time, for effective emittances that exceed unity. The resulting rms tempreature errors due to emittance uncertainties are 0.06, 0.04, and 0.85K for the infrared, split-window, and solar-infrared wavelengths, respectively. During the day, reflection of the incoming solar radition at the solar-infrared wavelengths must also be taken into account when computing the effective blackbody temperature of a scene. In extreme cases, the reflectance interpolation and emittance uncertainties together can result in solar infrared temperature errors that exceed 10K and 1K for ice and water-droplet clouds, respectively. For useful satellite angular configurations, the mean rms errors are less than 0.7K.

Specification of the visible optical depth, viewing and illumination conditions, clear-sky temperature at each wavelength, cloud temperature, and particle size, are the only parameters required to compute the radiances for the visible, solar infrared, infrared window, and split window in the absence of an atmosphere. When combined with the visible reflectance parameterization of Minnis et al. (1993b) and a representation of atmospheric gaseous absorption (e.g., Kratz, 1995), the parameterization can be used to simulate the top-of-the-atmosphere radiances for each wavelength. The limitations of the parameterizations developed here have been discussed and quantified in detail so that they may be applied confidently. Despite their shortcomings, these models are considerably more accurate and better understood than previous parameterizations. Because they are accurate and computationally economical, the models presented here should be valuable for simulating and retrieving cloud properties on a global scale.

Acknowledgments. Fred Denn of AS&M, Inc. provided the simulated satellite viewing angle calculations and

Bill Smith, Jr. of AS&M, Inc. prepared the satellite imagery. This research was supported by the Earth Observing System Interdisciplinary Program, NASA/Office of Mission to Planet Earth through the Clouds and Earth's Radiant Energy System Project. Additional support was provided by the Department of Energy Environmental Sciences Division, Inter Agency Transfer Agreement (ITF#21422116AQ through Pacific Northwest Laboratories and Inter Agency Agreement #DE-AI02-97ER62341 as part of the Atmospheric Radiation Measurement Program.

REFERENCES

Ackerman, S. A. and G. L. Stephens, 1987: The absorption of shortwave solar radiation by cloud droplets: an application of anomalous diffraction theory. *J. Atmos. Sci.*, **44**, 1574-1588.

Arking, A. and J. D. Childs, 1985: Retrieval of cloud cover parameters from multispectral satellite images. *J. Climate Appl. Meteor.*, **24**, 322-333.

Baum, B. A., R. F. Arduini, B. A. Wielicki, P. Minnis, and S. C. Tsay, 1993: Multilevel cloud retrieval using multispectral HIRS and AVHRR data: Nighttime oceanic analysis. *J. Geophys. Res.*, **99**, 5499-5514.

Coakley, J. A., Jr., R. L. Bernstein, and P. A. Durkee, 1987: Effect of ship-track effluents on cloud reflectivity. *Science*, **237**, 953-955.

Hale, G. M. and M. R. Querry, 1973: Optical constants of water in the 200-µm to 200-µm wavelength region. *Appl. Opt.*, **12**, 555-563.

Han, Q., 1992: Global survey of effective particle size in liquid water clouds. Ph.D. Dissertation, Columbia University, New York, NY, 199 pp.

____, Rossow, W. B., and A. A. Lacis, 1994: Near-global survey of effective droplet radii in liquid water clouds using ISCCP data. *J. Climate*. **7**, 465-497.

Hansen, J. E. and L. D. Travis, 1974: Light scattering in planetary atmospheres. *Space Sci. rev*., **16**, 527-610.

Heymsfield, A. J. and C. M. R. Platt, 1984: A parameterization of the particle size spectrum of ice clouds in terms of ambient temperature and ice water content. *J. Atmos. Sci.*, **41**, 846-855.

Heyney, L. C. and J. L. Greenstein, 1941: Diffuse radiation in the galaxy. *Astrophys. J.*, **93**, 70-83.

Inoue, T., 1985: On the temperature and effective emissivity determination of semi-transparent cirrus clouds by bi-spectral measurements in the 10 µm region. *J. Meteor. Soc. Japan*, **63**, 88-98.

Iqbal, M., 1983: Introduction to Solar Radiation. Academic Press, Toronto, Canada.

Kidwell, K. B., 1991: NOAA Polar Orbiter Data Users Guide (TIROS-N, NOAA-6, NOAA-7, NOAA-8, NOAA-9, NOAA-10, NOAA-11, and NOAA-12). NOAA/NESDIS, July. Available from NOAA/NESDIS, Princeton, Executive Sq., Rm. 100, Washington, DC, 20233.

Kratz, D. P., 1995: The correlated k-distribution technique as applied to the AVHRR channels. *J. Quant. Spectrosc. Radiat. Transfer*, **53**, 501-507.

Lee, T. F., 1989: Jet contrail identification using the AVHRR split window. *J. Appl. Meteorol.*, **28**, 993-995.

Liou, K. N., 1973: Transfer of solar irradiance through cirrus cloud layers. *J. Geophys. Res.*, **78**, 1409-1418.

_____, Y. Takano, S. C. Ou, A. Heymsfield, and W. Kreiss, 1990: Infrared transmission through cirrus clouds: a radiative model for target detection. *Appl. Opt.*, **29**, 1886-1896.

Macke, A., J. Mueller, and E. Raschke, 1996: Single scattering properties of atmospheric ice crystals. *J. Atmos. Sci.*, **53**, 2813-2825.

Minnis, P., P. W. Heck, and D. F. Young, 1993a: Inference of cirrus cloud properties from satellite-observed visible and infrared radiances. Part II: Verification of theoretical radiative properties. *J. Atmos. Sci*., **50**, 1305-1322.

_____, K. N. Liou, and Y. Takano, 1993b: Inference of cirrus cloud properties using satellite-observed visible and infrared radiances. Part I: Parameterization of radiance fields. *J. Atmos. Sci.*, **50**, 1279-1304.

_____, W. L. Smith, Jr., D. P. Garber, J. K. Ayers, and D. R. Doelling, 1995: Cloud properties derived from GOES-7 for the Spring 1994 ARM Intensive Observing Period using version 1.0.0 of the ARM satellite data analysis program. *NASA RP 1366*, August, 59 pp.

Ou, S. C., K. N. Liou, W. M. Gooch, and Y. Takano, 1993: Remote sensing of cirrus cloud parameters using Advanced Very High Resolution Radiometer 3.7- and 10.9-µm channels. *Appl. Opt.*, **32**, 2171-2180.

Parol, F., J. C. Buriez, G. Brogniez, and Y. Fouquart, 1991: Information content of AVHRR Channels 4 and 5 with respect to the effective radius of cirrus cloud particles. *J. Appl. Meteor.*, **30**, 973-984.

Poellot, M. R. and B. Henderson, 1994: University of North Dakota Citation FIRE Cirrus II Mission Summary and Data Report. Dept. of Atmos. Sci., University of North Dakota, Grand Forks, ND, March 15, 207 pp.

Radke, L. F., J. A. Coakley, Jr., M. D. King, 1989: Direct and remote sensing observations of the effects of ships on clouds. *Science*, **246**, 1146-1149.

Rossow, W. B., L. C. Garder, P. Lu, and A. Walker, 1988: International Satellite Cloud Climatology Project (ISCCP), Documentation of cloud data. *WCRP* Report WMO/TD-No. 266, 122 pp. [Available from Dr. W. B. Rossow at NASA Goddard Space Flight Center, Institute for Space Studies, 2880 Broadway, New York, NY, 10025.]

Stephens, G. L. and T. J. Greenwald, 1991: The Earth's radiation budget and its relation to atmospheric hydrology, 2, Observations of cloud effects. *J. Geophys. Res.*, **96**, 15,325-15,340.

Stokes, G. M. and S. E. Schwartz, 1994: The Atmospheric Radiation Measurement (ARM) Program: Programmatic background and design of the Cloud and Radiation Testbed. *Bull. Am. Meteorol. Soc.*, **75**, 1201-1221.

Stone, R. S., G. L. Stephens, C. M. R. Platt, 1990: The remote sensing of thin cirrus cloud using satellites, lidar, and radiative transfer theory. *J. Appl. Meteor.*, **29**, 353-366.

Takano, Y. and K. N. Liou, 1989: Radiative transfer in cirrus clouds: I. Single scattering and optical properties of oriented hexagonal ice crystals. *J. Atmos. Sci.*, **46**, 3-20.

_____, _____, and P. Minnis, 1992: The effects of small ice crystals on cirrus infrared radiative properties. *J. Atmos. Sci.*, **49**, 1487-1493.

Warren, S. G., 1984: Optical constants of ice from ultraviolet to the microwave. *Appl. Opt.*, **23**, 1206-1225.

Wiscombe, W. J., 1980: Improved Mie scattering algorithms. *Appl. Opt.*, **19**, 1505-1509.

APPENDIX

a. Effect of satellite sampling on VIS reflectance interpolation errors

Figure A1 shows the frequency distributions of Θ observed from several satellites that are currently or will be used to measure cloud properties. Only scattering angles corresponding to $\theta_o < 82°$ and $\theta < 70°$ were considered in these plots because few satellite-observed reflectances are interpreted at greater zenith angles. A scattering angle was computed for each 0.25° of latitude and longitude viewed by the satellite. For the GOES and the morning-orbit Earth Observing System (EOS-AM) satellite, the observations were restricted to latitudes equatorward of 60°. GOES observations were simulated every half hour for both the equinox and solstice days to cover the extremes of the solar positions. The EOS-AM satellite is assumed to be in a Sun-synchronous orbit with a 1030 Local Time descending node. The calculations were performed for the boreal summer and winter solstices and the autumnal equinox. The Tropical Rainfall Monitoring Mission (TRMM) satellite is in a 35°-inclined orbit with a repeat cycle of 47 days. The usual NOAA satellite orbits were simulated with equatorial crossing times of 0730 (AM) and 1430 LT (PM) for the same days as the EOS satellite.

Figure A1a shows that scattering angles between 140 and 175° are observed most often by GOES while $\Theta <$ 60° is viewed infrequently. During the equinoxes, the most common scattering angle is ~172°. This maximum shifts with solar declination to ~149° at the solstices. Larger scattering angles are not observed during the solstices because the line of sight from the sun through the satellite is off the Earth due to the height required for geostationary orbit. The maximum frequencies are near some of the angles with large errors (see Fig. 17) suggesting that the uncertainties in the modeled reflectance may be larger than the average given above. However, most of the angles with the largest reflectance errors are infrequently seen with the GOES geometry. A peak near 145° occurs for the EOS-AM (Fig. A1b) with a second maximum near $\Theta = 100°$. TRMM (Fig. A1c) has the most Gaussian distribution of all with a peak between 105° and 130°, a relatively flat section of the error distribution for water droplets but not for CS. The NOAA -AM (Fig. A1d) has a very pronounced maximum near 60° with a weak secondary peak near 155°. A strong backscattering peak is missing because the satellite often views a darker area with $\theta_o > 82°$ at that hour. NOAA-PM (Fig. A1e) is more like EOS-AM but with maxima closer to 90° and 160°.

The mean and rms errors for each satellite configuration were recomputed by weighting each simulated observation by the appropriate frequency in Fig. A1. The results are summarized in Table A1. In most cases, the mean and rms errors are less than expected for no satellite-view weightings. Mean reflectances are greatest for the unweighted cases because the reflectances at small values of Θ are much larger than those at other angles. For water droplets, the reflectance uncertainties due to interpolation are smallest for the NOAA-AM orbits and greatest for the GOES and EOS-AM observations. The water-droplet errors and most of the satellite observations occur at $\Theta >$ 60° (see Fig. 17a). Therefore, the satellite and unweighted rms errors are not very different. The ice-model errors for the satellite viewing geometries are all significantly less than the unweighted errors due to the lack of observations at the smaller scattering angles. Because of fixed viewing geometry for a given area, the interpolation errors from GOES will probably not average out the bias for a given local time. The daily average error may approach zero, however, when all local hours are considered because of the wide range of Θ observed over the day. The other satellites view a particular area from a different angle each day, therefore, the mean error incurred at one scattering angle will likely be compensated to some extent by views from other angles on subsequent days. For example, during its 11-day repeat cycle, the AVHRR cross-track scanner views a particular area toward and away from the sun over a θ-range of $\pm$ 70° giving a large range in Θ. While other satellite-solar configurations are expected to differ from those considered here (e.g., Fig. A1), it is apparent that views at $\Theta <$ 50° will be relatively infrequent. Thus, the sharp halo features in the VIS ice crystal phase functions will rarely be a factor in the retrieval of cloud properties. However, the large reflectance errors expected for $\Theta >$ 174° will be encountered in the views from most satellites. Users of these models should be aware of the potential errors in these situations.

b. SI temperature errors due to interpolation

An independent datset was created to determine the SI temperature errors due to the parameterizations and interpolations of emittance. The AD computations were performed for the T40 and 8-μm models using 9 solar zenith, 9 viewing zenith, and 10 relative azimuth angles, 7 optical depths, 5 surface albedos ranging from 0 to 0.20, and with and without the solar component. The angles were selected to cover the full range of useful viewing and illumination conditions while differing from the lookup table nodes. One set of optical depths was selected to be approximately midway between the interpolation nodes and the other corresponds to the VIS model nodes. Five combinations of T_C and T_S were selected for the ice and liquid model calculations to cover a realistic range of values. For T40, T_C/T_S = 222K/283K, 203K/309K. 236K/268K, 264K/283K, and 257/309K. The last three combinations were also used for the 8-μm model in addition to T_C/T_S = 281K/309K and 287K/293K.

1) NIGHTTIME ERRORS

The off-node rms errors in the effective emittance parameterization for channel 3 in ε are 1.1% and 2.5% for the 8-μm and T40 models, respectively, similar to the SEEs from the regression fits. Assuming that the results are typical of all of the models in this study, it can be concluded that the SEEs in Fig. 13 are representative of the parameterization errors for each of the six wavelengths.

For the T40 cases, the no-sun comparisons produced temperature errors of -0.1 $\pm$ 1.1K for values of τ between the optical depth nodes. At the nodes, the errors are 0 $\pm$ 0.3K. The mean optical depth interpolation error can be estimated using the rms mean which is 0 $\pm$ 1.0K for the T40 model. For the 8-μm data, the rms off- and on-node errors are 0.5 and 0.6K, respectively. Thus, the Lagrangian interpolation introduces almost no additional error for the 8-μm model. Most of the uncertainty arises for the thick, high cirrus cases where ΔT_{SC}, is greatest. For $\tau < 8$, the off-node T40 rms errors are only 0.3 K, but 2.2 K for $\tau > 8$.

To further illustrate the sensitivity to ΔT_{SC}, consider the case for the T40, 3.75-μm model where $\tau = 12.2$, the parameterized emittance error is 0.002, T_S = 309K, and T_C = 203K. This small emittance error (~0.2%) translates to a temperature error of -10K because the sensitivity factor is so large. Although the temperature errors at the optical depth nodes are only ~1K, the small interpolation error in emittance produces a large temperature error. Thus, the simulation of top-of-the-atmosphere SI temperatures for high-altitude cirrus over hot land surfaces can be subject to some significant uncertainties despite the small effective emittance errors. The IR and WS temperature errors are much smaller than the SI values because the magnitudes of $\Delta R/R$ in (13) are generally much less than the SI values.

In most cases, the SI temperature estimates from these parameterizations will be within $\pm$0.5K of the AD model results. Although the accuracy of this model exceeds that of previous parameterizations, especially for the SI spectra, there are some situations that will result in large temperature errors and, for remote sensing, large retrieval uncertainties. To minimize the effect of the sensitivity to emittance interpolation in high contrast situations, it may be more accurate to interpolate using the TOA temperatures at the nodes. Using temperature instead of emittance as the dependent variable in the interpolation decreases the errors to 1.0 K for $\tau > 8$ for the T40 case, but does not decrease the errors for $\tau < 8$ or for the 8-μm model. Because it requires many fewer calculations, emittance interpolation is preferred. The largest errors could be reduced, however, if temperature interpolation were employed for larger ice-cloud optical depths only. For example, the overall T40 interpolation error is 0.6K if temperature and emittance interpolations are used for $\tau > 8$ and $\tau < 8$, respectively.

2) DAYTIME ERRORS

The uncertainties in the daytime SI temperatures may be greater than those at night because of the interpolation errors between the reflectance model nodes. The temperature errors were computed for the 8-μm and T40 models during the daytime for a surface albedo of 0.05. Overall, there is no bias in the 8-μm results with an rms error of 0.6 K, the same as the emittance-only errors. Thus, the Lagrangian interpolation yields negligible errors for the smooth 8-μm SI phase function. The features in the ice-crystal phase function, however, appear to introduce some substantial uncertainty into the estimation of SI temperature during the daytime. Although 86% of the errors are smaller than $\pm$ 1K, nearly 2.5% of the simulated temperatures differ by more than 10K from their AD counterparts.

The errors are plotted in Fig. A2 as means and standard deviations for each 5° of scattering angle. In Fig. A2a, it is clear that the greatest errors for the 8-μm model are incurred for $\Theta > 155°$ with the maximum error of -1.0 $\pm$ 1.2K. The T40 errors (Fig. A2b) are greatest in the backscattering direction, but they are much larger than the corresponding 8-μm values. Significant errors also occur for T40 in the forward scattering directions for $\Theta < 50°$. Between 50 and 140°, the interpolation errors are negligible. Thus, for most of the angles commonly observed by satellites (e.g., Fig. A1), the parameterized daytime SI temperatures will be within $\pm$ 0.7K of the AD values, especially for the water droplet model. For the ice crystal models, the user should take into account the potentially large errors in the SI cloud temperatures for $\Theta > 150°$. Overall, the rms error for the T40 daytime results is ~$\pm$ 1.0K.

The SI temperature errors for the other simulated surface albedos are almost identical to those found for a surface albedo of 0.05. Thus, the parameterization represented by (11) accurately accounts for the underlying surface. The two models used in this error analysis are in the middle of the considered size distributions and the results should represent an average parameterization error for all of the particle sizes. Both greater and smaller errors will be encountered for a given particle size, however, depending on the variations in the scattering phase function.

Satellite/Channel	Nominal Wavelength (mm)	index of refraction water	index of refraction ice
GOES/visible, AVHRR/1	0.65	1.331 - i1.64x10^{-8}	1.308 - i1.44x10^{-8}
GOES/2	3.90	1.356 - i0.00398	1.372 - i0.00817
AVHRR/3	3.75	1.370 - i0.00408	1.396 - i0.00779
GOES/4	10.7	1.173 - i0.08071	1.115 - i0.16520
AVHRR /4	10.8	1.162 - i0.09143	1.089 - i0.18300
GOES/5	12.0	1.117 - i0.19641	1.274 - i0.40440
AVHRR /5	11.9	1.118 - i0.18910	1.258 - i0.40900

Table 1. Refractive indices used for Mie and spheroid calculations.

MODEL	Q (VIS)	$\tilde{w}_o$ (VIS)	g (VIS)	Q (3.90/ 3.75 μm)	$\tilde{\omega}_o$ (3.90/ 3.75 μm)	g (3.90/ 3.75 μm)
C5	2.1097	1.0000*	0.7607	3.1520 / 3.4140	0.9533 / 0.9558	0.7559 / 0.7473
C10.5	2.1094	1.0000*	0.8048	3.4569 / 3.6388	0.9488 / 0.9441	0.7893 / 0.7783
C10	2.0582	1.0000*	0.7662	2.7075 / 2.4580	0.9017 / 0.8772	0.7601 / 0.7344
C20	2.0291	1.0000*	0.7704	2.3253 / 2.1853	0.7960 / 0.7893	0.8060 / 0.7981
C50	2.0134	1.0000*	0.7780	2.1042 / 2.1292	0.6814 / 0.6821	0.8834 / 0.8764
C120	2.0038	1.0000*	0.8155	2.0839 / 2.0715	0.6226 / 0.6229	0.9305 / 0.9258
C300	2.0000	1.0000*	0.8429	2.0424 / 2.0361	0.5749 / 0.5774	0.9531 / 0.9492
C750	2.0000	1.0000*	0.8592	2.0217 / 2.0185	0.5487 / 0.5516	0.9621 / 0.9584

Table 2. Monodisperse ice cloud optical properties for GOES VIS and AVHRR channel 1 and for GOES channel 2 and AVHRR channel 3. *Actual values between 0.99999243 and 0.99999929.

MODEL	Q	$\widetilde{\omega}_o$	g
C5	0.6555 / 0.6876	0.1381 / 0.1274	0.5144 / 0.5039
C10.5	0.8567 / 0.8738	0.1865 / 0.1734	0.6855 / 0.6764
C10	1.1741 / 1.1800	0.2749 / 0.2578	0.8298 / 0.8261
C20	1.7484 / 1.7193	0.4088 / 0.3998	0.9328 / 0.9346
C50	2.0709 / 2.0133	0.4870 / 0.4828	0.9678 / 0.9620
C120	2.100 / 2.0726	0.5079 / 0.5111	0.9770 / 0.9736
C300	2.0467 / 2.0378	0.5100 / 0.5120	0.9772 / 0.9737
C750	2.0239 / 2.0127	0.5101 / 0.5120	0.9781 / 0.9760

Table 3. Monodisperse ice cloud optical properties for GOES / AVHRR channels 4.

MODEL	Q	$\widetilde{\omega}_o$	g
C5	1.3682 / 1.3717	0.2290 / 0.2263	0.4556 / 0.4588
C10.5	1.6757 / 1.6710	0.2919 / 0.2886	0.6295 / 0.6327
C10	2.0365 / 2.0199	0.3803 / 0.3769	0.7849 / 0.7865
C20	2.2922 / 2.2616	0.4700 / 0.4710	0.8919 / 0.8942
C50	2.2279 / 2.2149	0.5165 / 0.5180	0.9284 / 0.9290
C120	2.1770 / 2.1684	0.5256 / 0.5276	0.9388 / 0.9396
C300	2.0968 / 2.0961	0.5253 / 0.5273	0.9554 / 0.9564
C750	2.0496 / 2.0492	0.5252 / 0.5272	0.9751 / 0.9760

Table 4. Monodisperse ice cloud optical properties for GOES/AVHRR channels 5.

MODEL	D_e (μm)	V (x 10^{-2} μm^3)	A (x 10^{-3} μm^2)
NCON	5.83	2.943	3.777
CON	18.15	15.49	10.04
CC	23.86	68.90	47.26
T60	30.36	110.2	58.10
CS	41.20	278.7	103.3
WCS	45.30	243.9	82.57
T40	67.6	538.0	123.0
NOV	75.2	1700	314.4
OCT	104.9	3379	436.5
CU	123.1	5730	611.0
LPC	134.9	17244	1654

Table 5. Ice cloud model physical properties.

Model / λ	0.65	3.73	3.90	10.7	10.8	11.9	12.0
r_e (μm)							
2	0.8012	0.7901	0.7908	0.4096	0.4204	0.3405	0.3358
4	0.8455	0.7914	0.8101	0.7578	0.7546	0.7103	0.7061
6	0.8582	0.7532	0.7700	0.8594	0.8585	0.8335	0.8308
8	0.8653	0.7727	0.7771	0.9022	0.9023	0.8849	0.8829
12	0.8725	0.8244	0.8281	0.9375	0.9386	0.9281	0.9267
16	0.8772	0.8499	0.8566	0.9513	0.9531	0.9460	0.9447
32	0.8842	0.8953	0.9038	0.9689	0.9712	0.9673	0.9664
ice							
NCON	0.778	0.7586	0.7703	0.6869	0.6856	0.6257	0.6234
CON	0.769	0.7705	0.7853	0.9088	0.9073	0.8412	0.8390
CC	0.772	0.8057	0.8134	0.9382	0.9391	0.8988	0.8966
T60	0.777	0.8216	0.8291	0.9475	0.9468	0.9071	0.9053
CS	0.785	0.8571	0.864	0.9616	0.9584	0.9221	0.9210
WCS	0.787	0.84690	0.8538	0.9577	0.9557	0.9193	0.9179
T40	0.802	0.87310	0.8793	0.9652	0.9626	0.9309	0.9297
NOV	0.817	0.91208	0.9173	0.9732	0.9698	0.9423	0.9413
OCT	0.832	0.92512	0.9299	0.9744	0.9714	0.9520	0.9519
CU	0.840	0.93436	0.9367	0.9756	0.9728	0.9603	0.9593
LPC	0.848	0.94763	0.9517	0.9772	0.9746	0.9660	0.9650

Table 6. Asymmetry factors g for model particle size distributions.

Model / λ	3.73	3.90	10.7	10.8	11.9	12.0
r_e (μm)						
2	0.9762	0.9699	0.1831	0.1556	0.0945	0.0941
4	0.9622	0.9577	0.3593	0.3166	0.2109	0.2104
6	0.9308	0.9237	0.4558	0.4109	0.2893	0.2886
8	0.9052	0.8930	0.5092	0.4659	0.3415	0.3407
12	0.8685	0.8509	0.5546	0.5178	0.4030	0.4020
16	0.8381	0.8174	0.5617	0.5323	0.4350	0.4342
32	0.7451	0.7194	0.5162	0.5092	0.4790	0.4791
ice						
NCON	0.9407	0.9449	0.1918	0.1777	0.2847	0.2880
CON	0.8401	0.8531	0.3685	0.3556	0.4192	0.4203
CC	0.7849	0.7882	0.4191	0.4110	0.4762	0.4751
T60	0.7585	0.7624	0.4379	0.4315	0.4862	0.4849
CS	0.7057	0.7104	0.4704	0.4667	0.5055	0.5040
WCS	0.7176	0.7214	0.4606	0.4566	0.4988	0.4974
T40	0.6775	0.6804	0.4780	0.4763	0.5087	0.5072
NOV	0.6281	0.6304	0.4989	0.4997	0.5215	0.5198
OCT	0.6034	0.6038	0.5018	0.5028	0.5227	0.5209
CU	0.5875	0.5868	0.5042	0.5054	0.5234	0.5221
LPC	0.5706	0.5693	0.5084	0.5102	0.5265	0.5246

Table 7. Single-scattering albedos $\tilde{\omega}_o$ for model particle size distributions.

Model / λ	0.65	3.73	3.90	10.7	10.8	11.9	12.0
r_e (μm)							
2	2.277	2.466	2.226	0.314	0.335	0.539	0.552
4	2.191	3.180	3.240	0.739	0.749	0.977	0.995
6	2.143	2.564	2.647	1.176	1.156	1.310	1.327
8	2.118	2.387	2.405	1.550	1.499	1.545	1.559
12	2.090	2.298	2.307	2.066	1.973	1.835	1.843
16	2.074	2.243	2.251	2.307	2.208	1.982	1.985
32	2.029	2.149	2.154	2.301	2.271	2.119	2.119
ice							
NCON	2.101	3.329	3.188	0.824	0.846	1.600	1.603
CON	2.049	2.486	2.554	1.480	1.410	2.028	2.110
CC	2.027	2.296	2.300	1.816	1.752	2.254	2.282
T60	2.023	2.236	2.253	1.875	1.815	2.241	2.267
CS	2.016	2.173	2.164	1.9874	1.935	2.216	2.235
WCS	2.018	2.195	2.191	1.943	1.892	2.214	2.237
T40	2.012	2.144	2.143	1.988	1.947	2.183	2.212
NOV	2.006	2.084	2.086	2.050	2.021	2.151	2.192
OCT	2.004	2.063	2.065	2.035	2.014	2.116	2.132
CU	2.002	2.049	2.051	2.031	2.012	2.094	2.105
LPC	2.001	2.033	2.036	2.036	2.022	2.078	2.088

Table 8. Extinction efficiency factors Q for model particle size distributions.

Model	Error (%)	Nearest Node	Linear Interpolation	Hybrid Interpolation	Lagrangian 4-point Interpolation
8 μm	bias	-0.3	-0.9	-0.5	-0.4
	rms	21.8	4.9	3.0	2.9
CS	bias	0.7	-0.3	0.1	0.2
	rms	19.0	11.1	9.9	10.1

Table 9. Reflectance errors due to interpolation between angle nodes.

Model	3.75-μm ΔT (K)		3.90-μm ΔT (K)	
r_e (μm)	all	$\varepsilon < 1$	all	$\varepsilon < 1$
2	1.16	0.71	1.07	0.67
4	1.21	0.69	1.16	0.69
6	1.02	0.55	1.00	0.57
8	0.81	0.48	0.81	0.48
12	0.55	0.36	0.55	0.37
16	0.42	0.30	0.42	0.30
32	0.22	0.18	0.22	0.18
ice distribution				
NCON	2.44	1.13	2.20	0.84
CON	1.62	1.04	1.45	0.90
CC	1.22	0.75	1.04	0.64
T60	1.06	0.62	0.90	0.56
CS	0.92	0.54	0.81	0.42
WCS	0.83	0.44	0.70	0.37
T40	0.63	0.32	0.52	0.27
NOV	0.45	0.26	0.38	0.19
OCT	0.32	0.17	0.25	0.13
CU	0.27	0.15	0.21	0.11
LPC	0.21	0.12	0.16	0.09

Table 10. RMS temperature differences between AD model and emittance parameterization.

Satellite/Month	8-μm droplet			CS		
	Mean Reflectance	mean error (%)	rms error (%)	Mean Reflectance	mean error (%)	rms error (%)
no satellite	0.586	-0.51	3.0	0.628	0.12	9.9
GOES/Sept.	0.464	-0.37	3.2	0.551	0.21	3.5
GOES/Dec.	0.465	-0.36	3.1	0.542	0.40	3.4
EOSAM/June	0.437	-0.21	3.3	0.511	0.03	1.9
EOS-AM/Sept.	0.441	-0.30	3.5	0.510	0.09	2.1
EOS-AM/Dec.	0.443	-0.36	3.1	0.531	0.16	2.0
TRMM/Apr.	0.436	-0.36	3.1	0.526	0.01	1.6
TRMM/Dec.	0.452	-0.43	3.0	0.543	0.02	2.5
NOAA-1430/June	0.458	-0.33	2.8	0.576	0.22	2.0
NOAA-1430/Sept.	0.456	-0.35	2.9	0.573	0.19	2.1
NOAA-1430/Dec.	0.447	-0.37	2.8	0.556	0.34	2.1
NOAA-0730/June	0.568	-0.66	2.6	0.651	-0.08	5.1
NOAA-0730/Sept.	0.542	-0.67	2.5	0.646	-0.27	3.7
NOAA-0730/Dec.	0.521	-0.60	2.6	0.630	-0.07	3.0

Table A1. Reflectance interpolation errors convolved with the scattering angle frequencies in Fig. 15 for various satellite configurations.

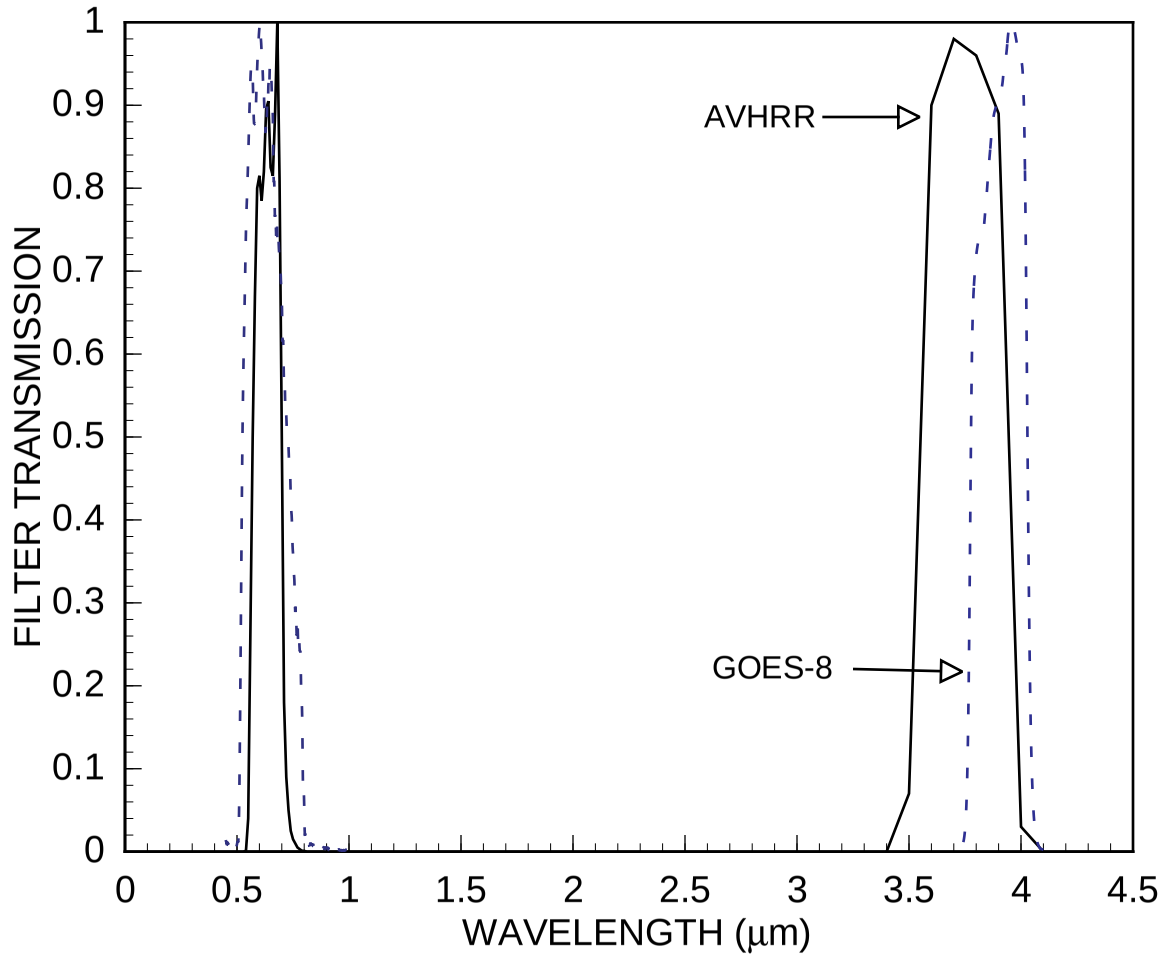

Fig. 1a. Filter functions for GOES-8 (dashed) and AVHRR (solid) visible and solar-infrared channels.

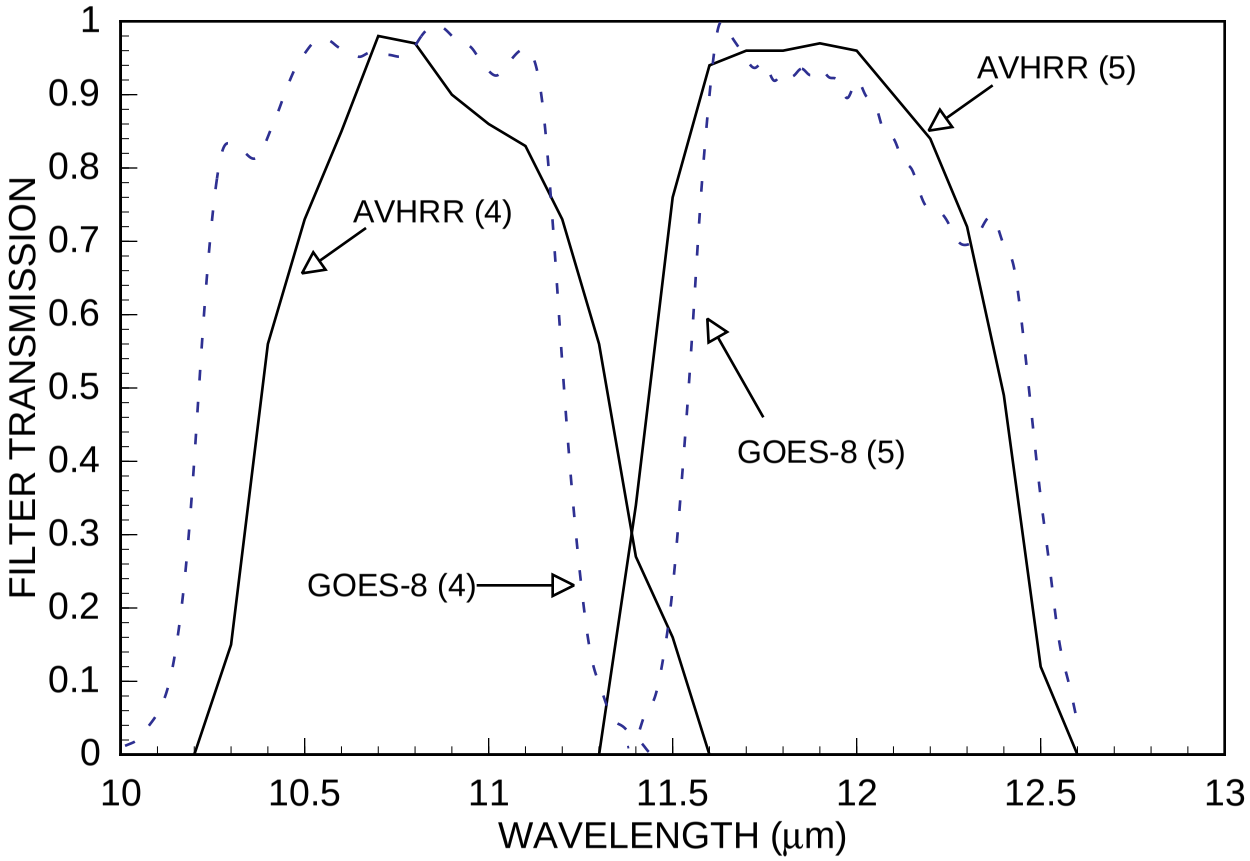

Fig. 1b. Filter functions for GOES-8 (dashed) and AVHRR (solid) split window channels in the thermal infrared spectrum.

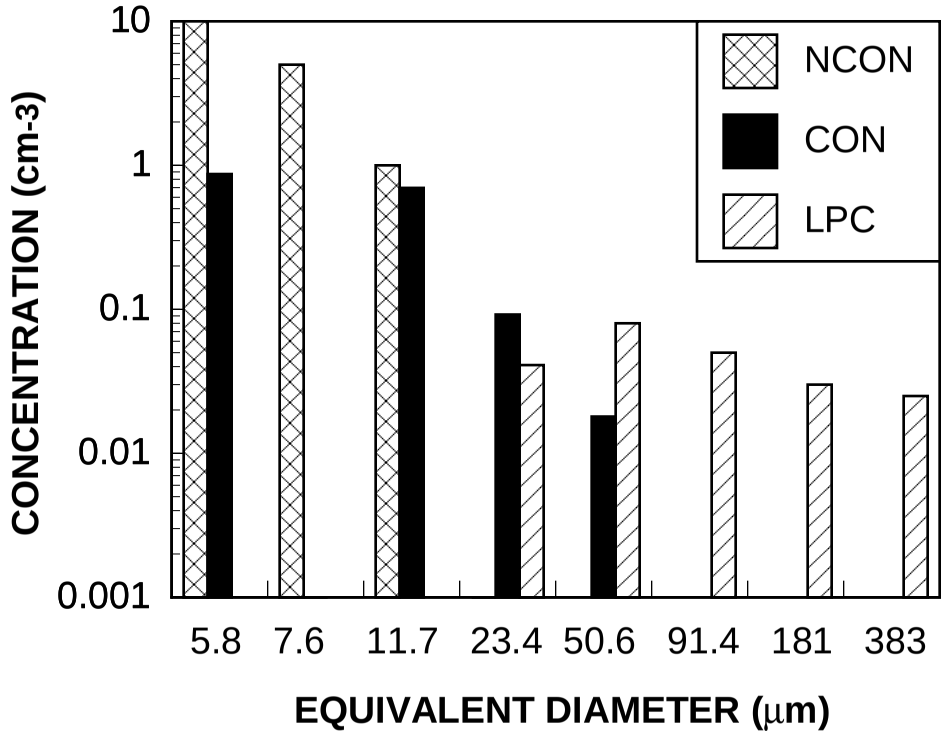

Fig. 2. Ice crystal distributions developed for a new contrail (NCON), an older contrail (CON), and a large-particle cirrus (LPC) cloud.

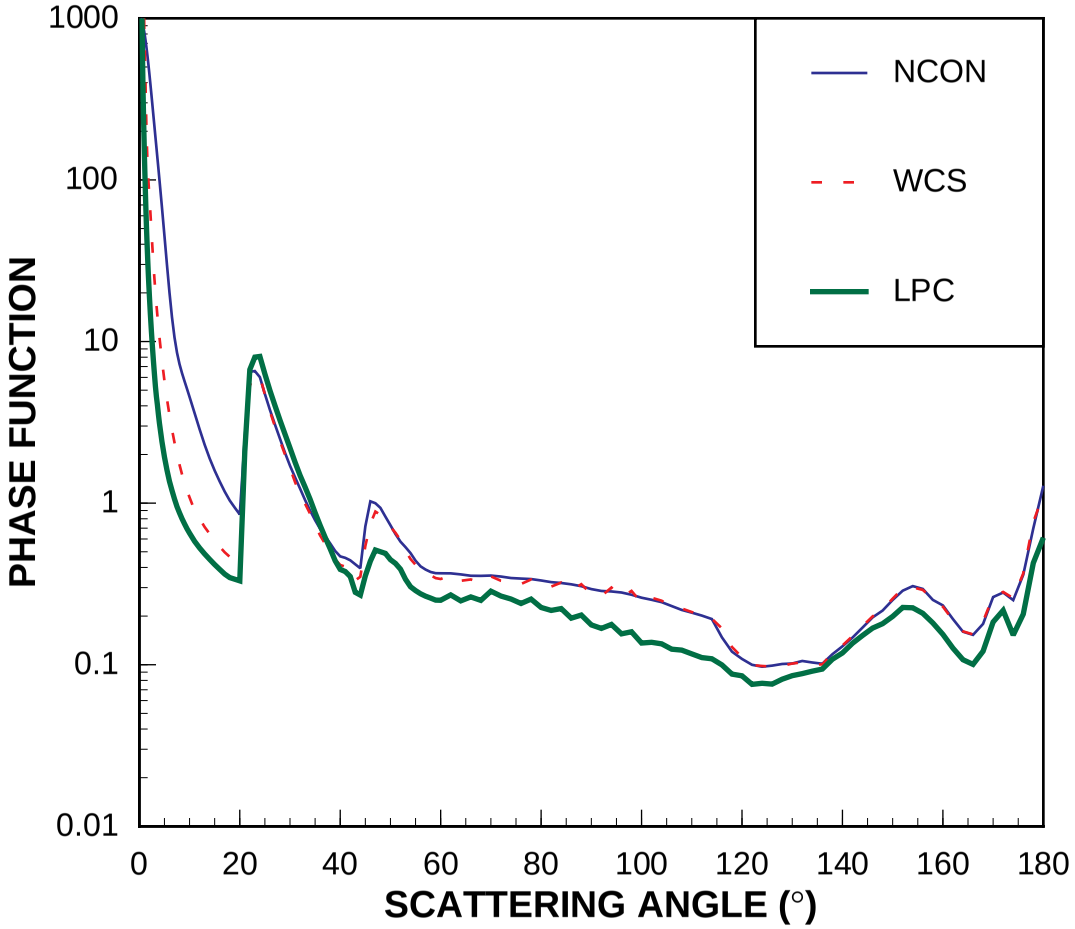

Fig. 3a. Scattering phase function for $\lambda = 0.65$ μm for three different ice cloud models (forward scattering maxima have been clipped).

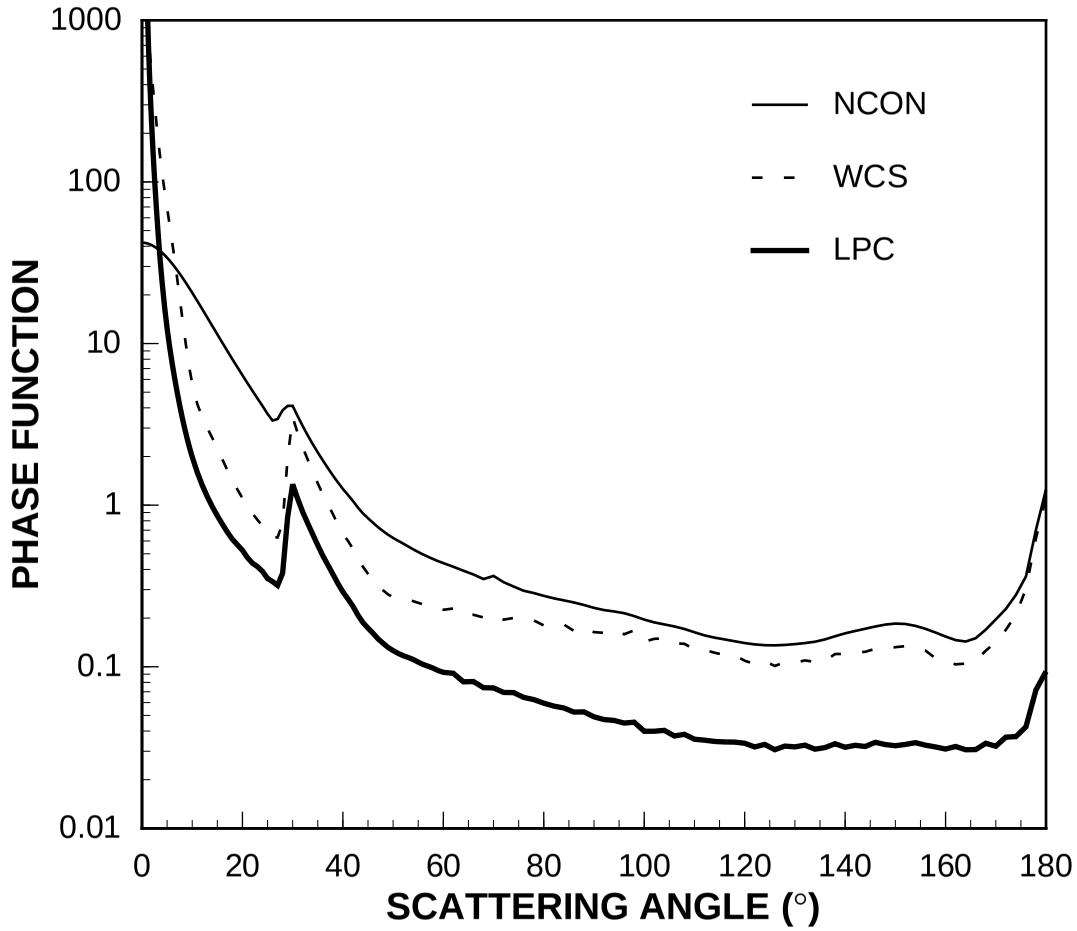

Fig. 3b. Scattering phase function for $\lambda = 3.75$ μm for three different ice cloud models (forward scattering maxima have been clipped).

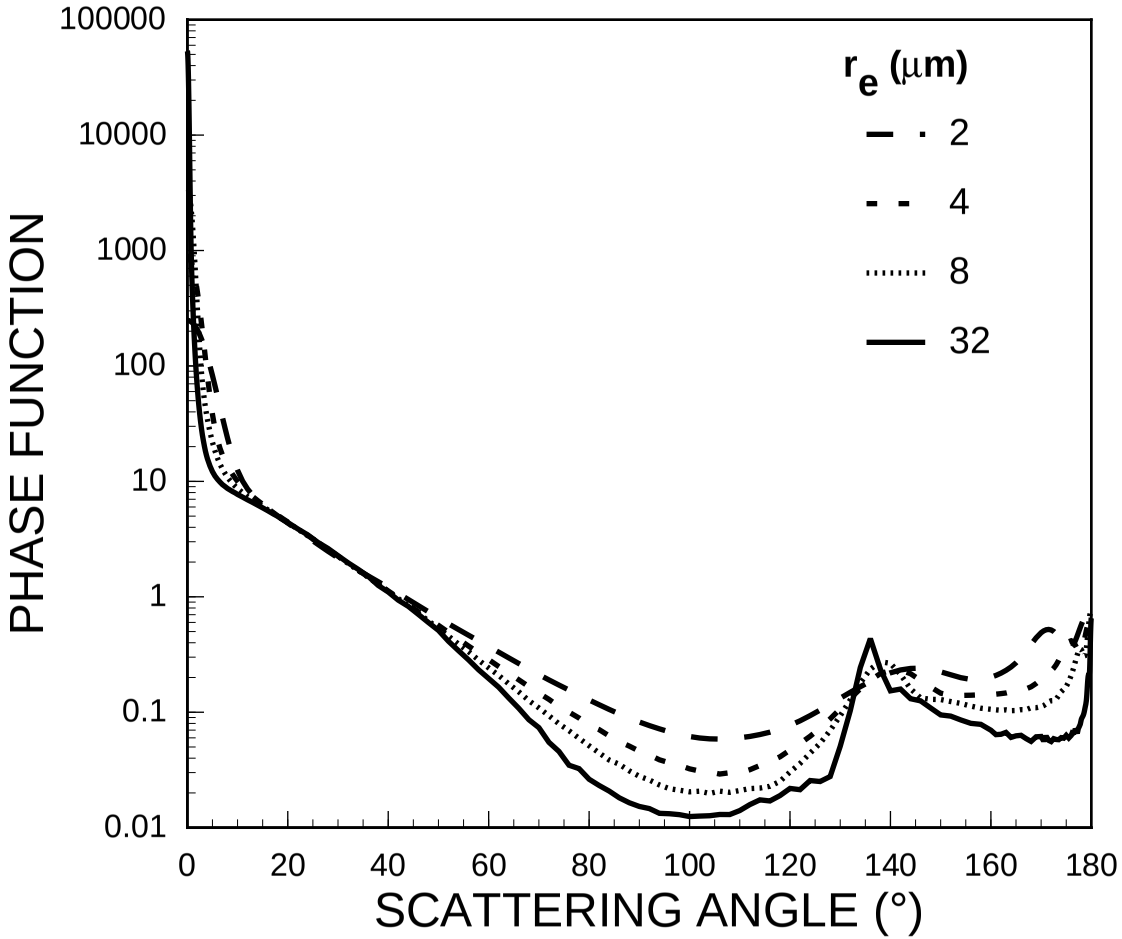

Fig. 4a. Theoretical Mie scattering phase functions at $\lambda = 0.65\ \mu m$ for modified gamma distributions of water droplets.

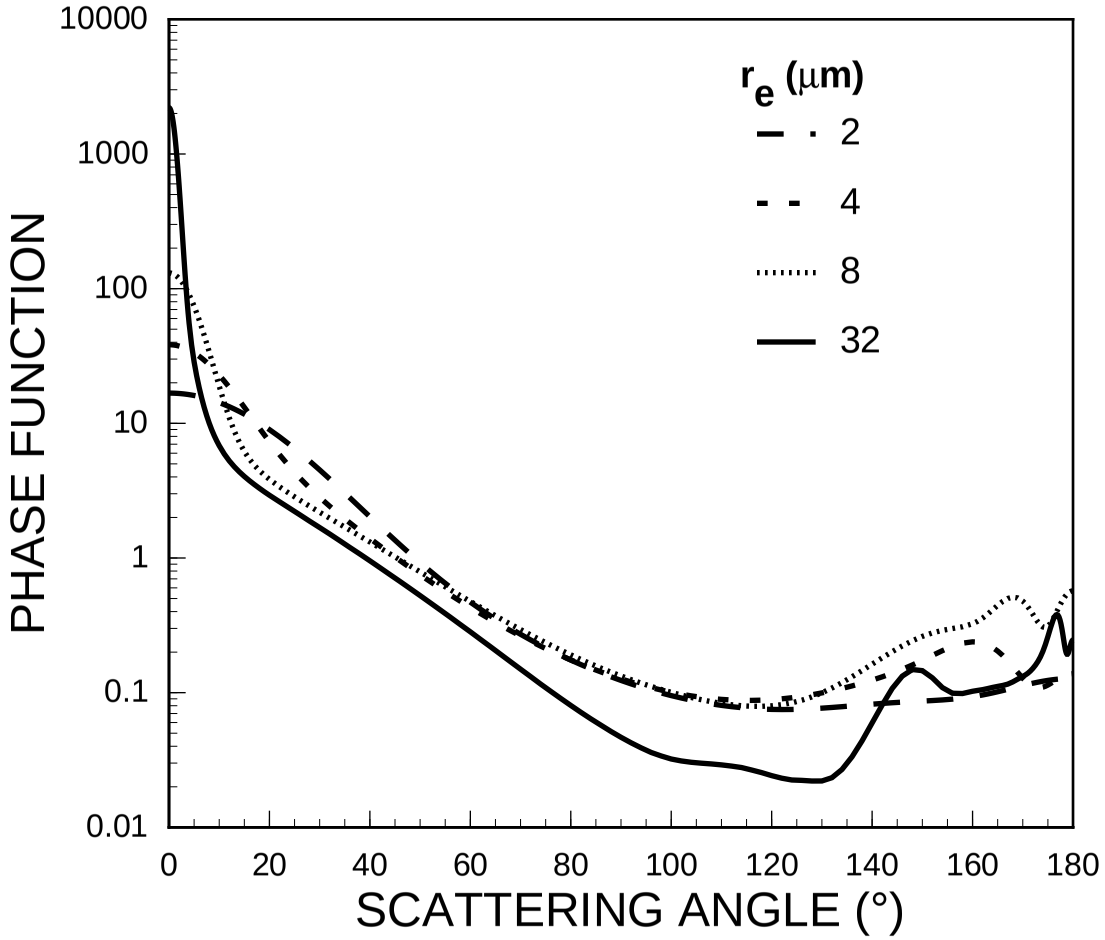

Fig. 4b. Mie-scattering phase functions at $\lambda = 3.75\ \mu m$ for modified gamma distributions of water droplets.

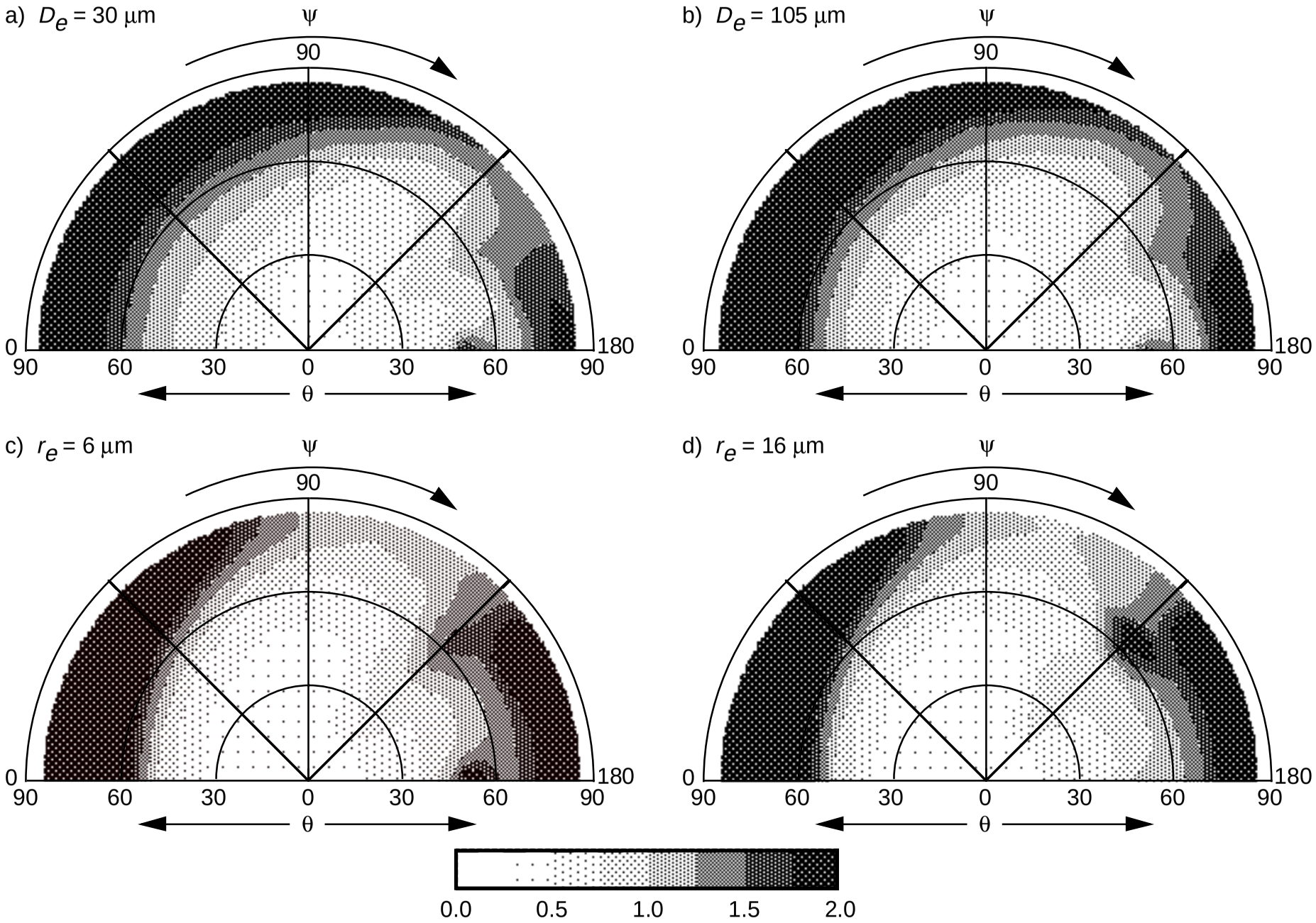

Fig. 5. Anisotropic reflectance factors for λ = 0.65 μm, μ_o = 0.65, and τ = 1.0.

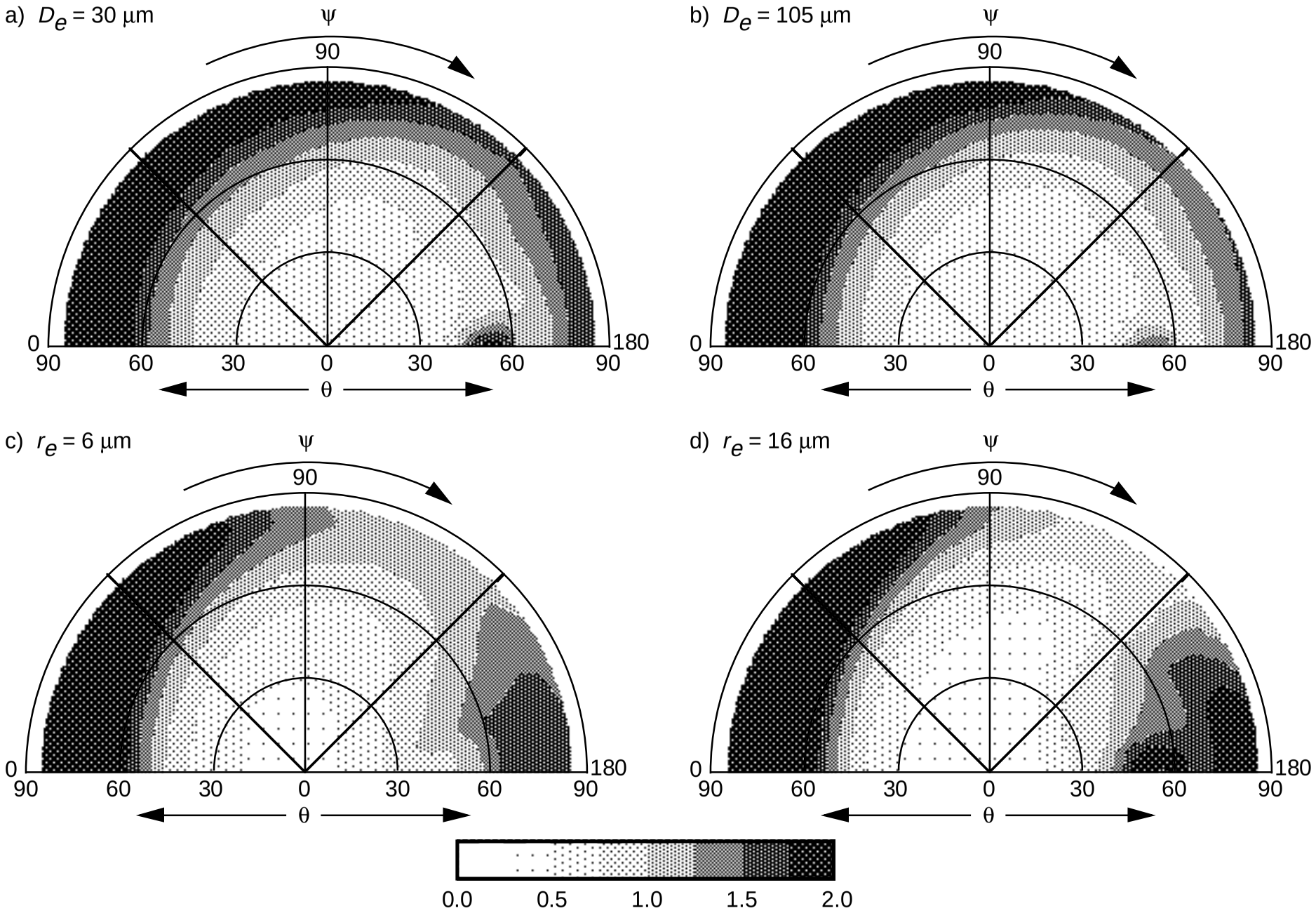

Fig. 6. Same as Fig. 5, but for λ = 3.75 μm.

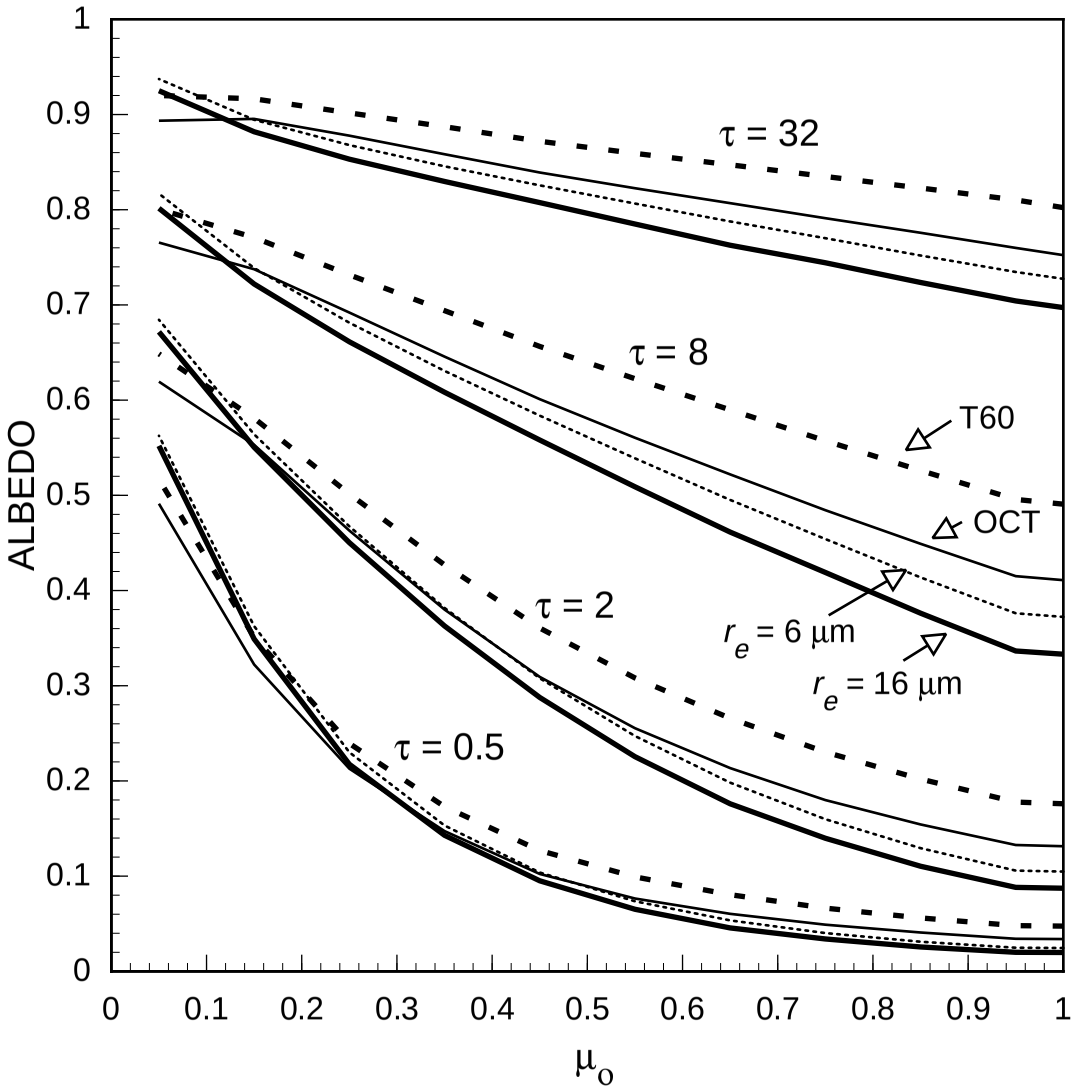

Fig. 7. Solar zenith angle dependence of albedo at $\lambda = 0.65$ μm.

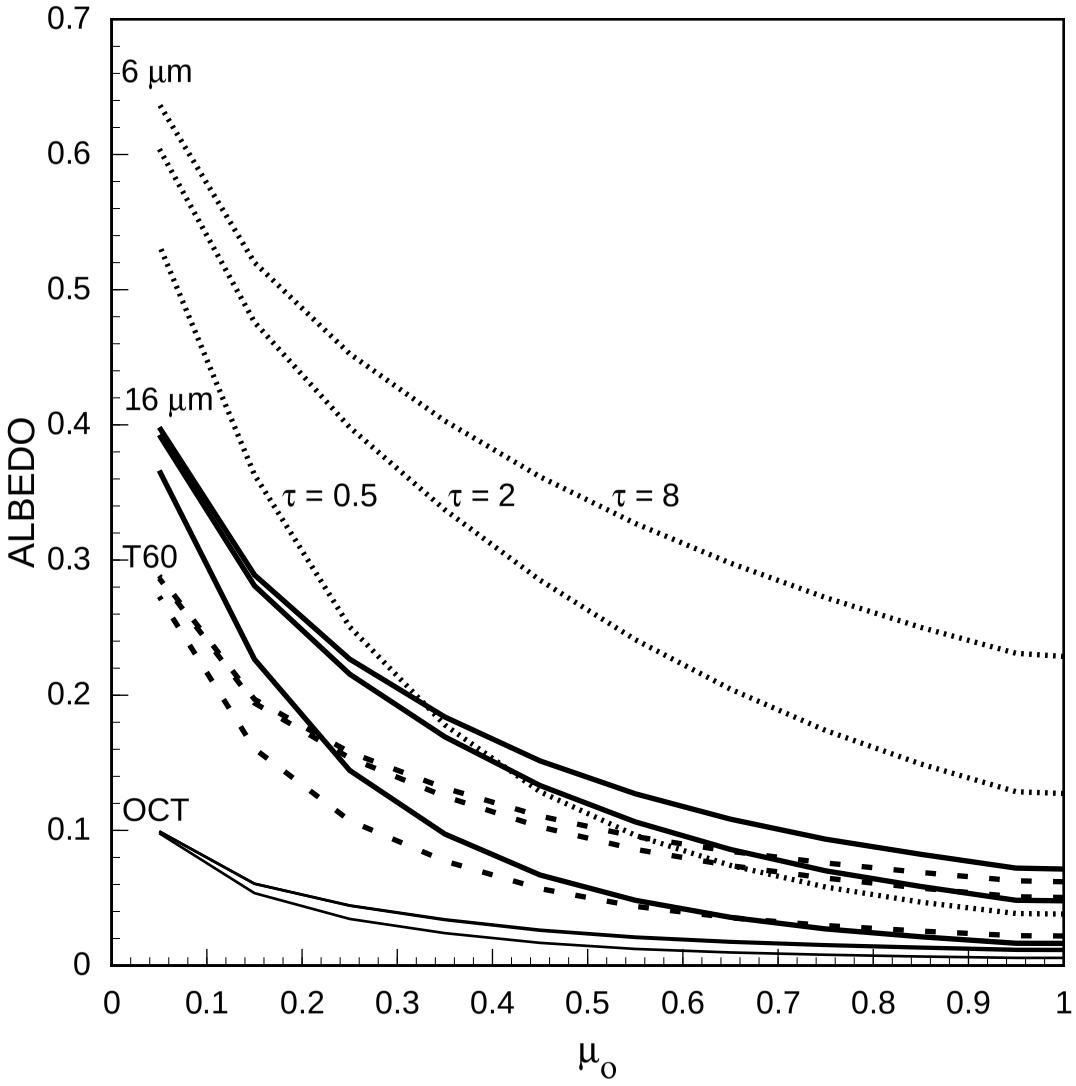

Fig. 8. Solar zenith angle dependence of cloud albedo at $\lambda = 3.75\ \mu$m.

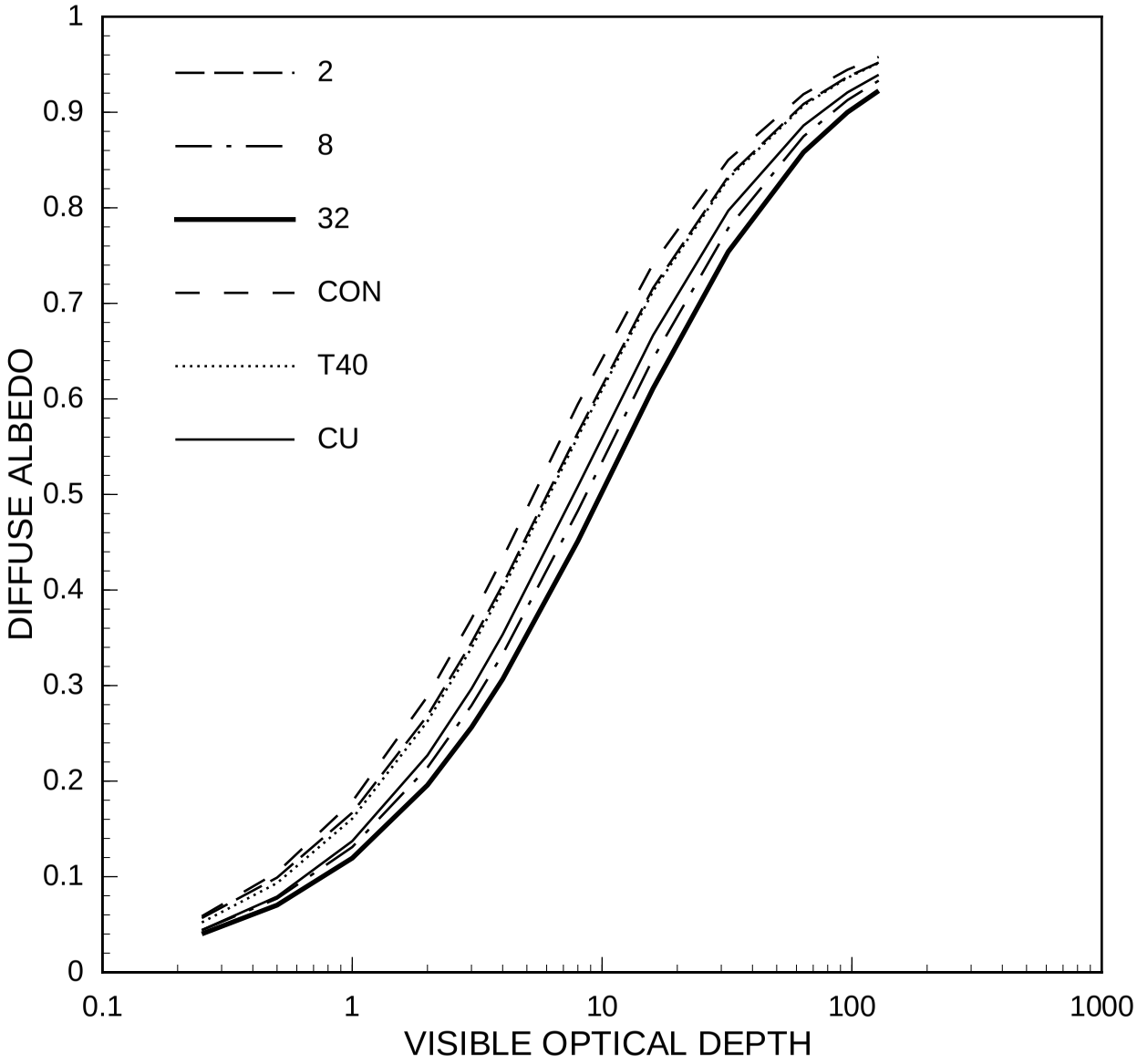

Fig. 9. Diffuse albedos for model clouds at $\lambda = 0.65$ μm.

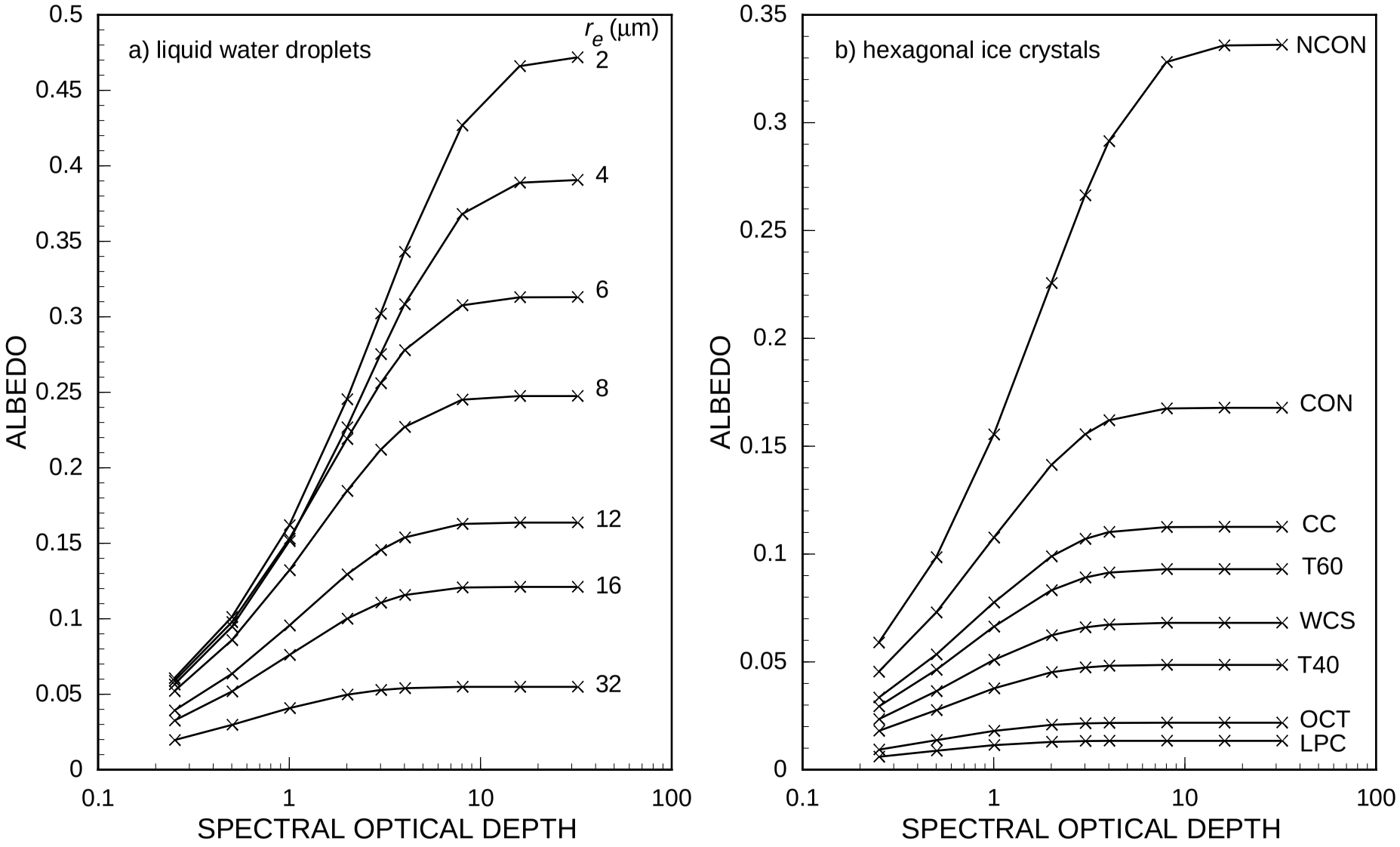

Fig. 10. Diffuse albedo for model clouds at $\lambda = 3.75\ \mu$m. [Note scale differences between (a) and (b).]

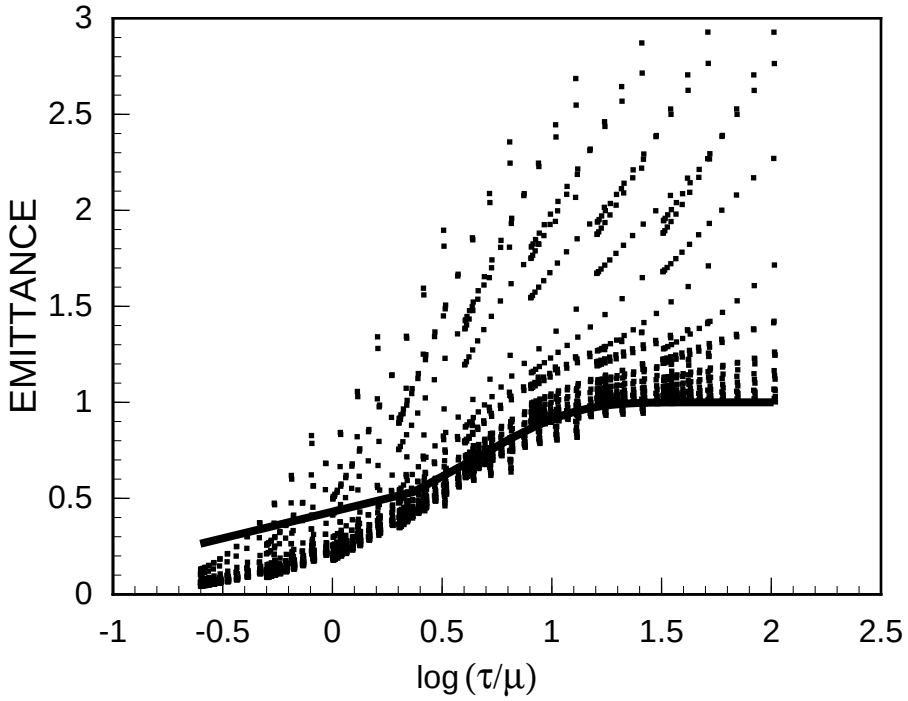

(a) AVHRR channel-3, 3.75μm.

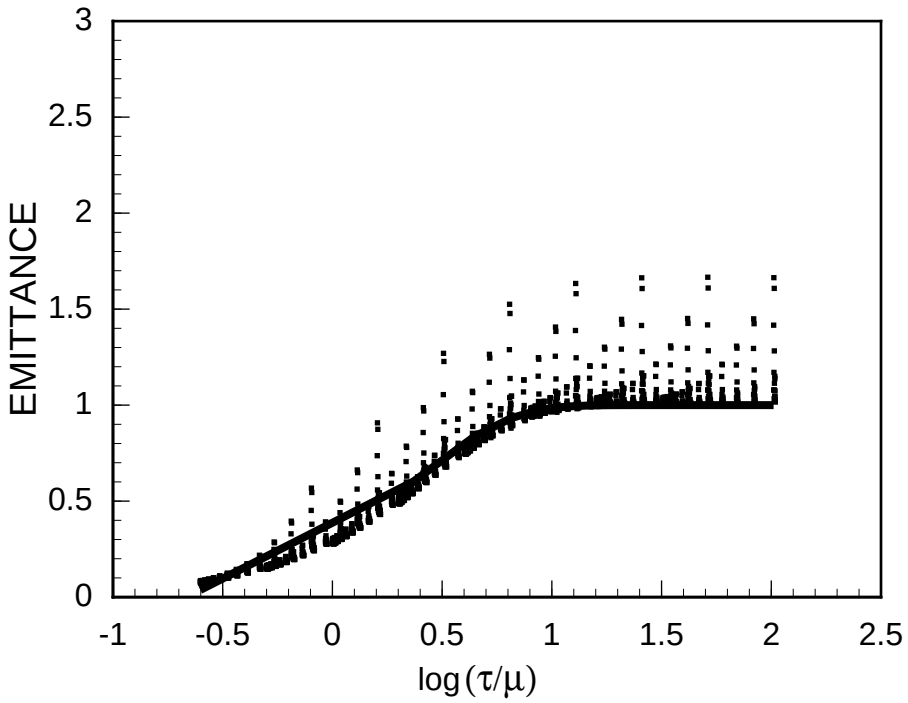

(b) AVHRR channel-4, 10.8μm.

Figure 11. Effective emittances for all calculations at $r_e = 6\ \mu$m and a regression fit of $\varepsilon = 1 - \exp[\ (a\ \tau/\mu)^b\ ]$.

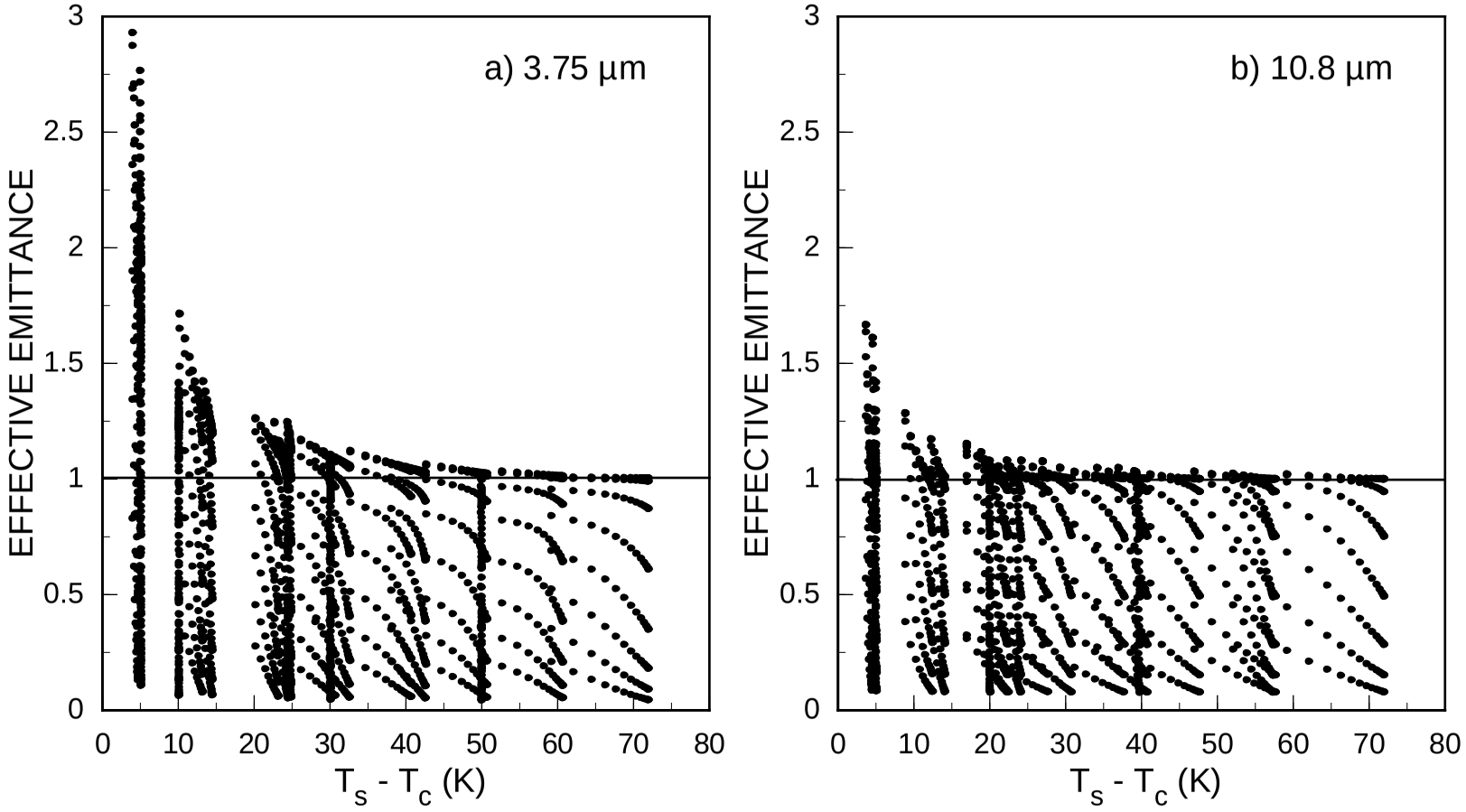

Fig. 12. Variation of effective emittance with clear-cloud temperature difference from adding-doubling model calculations for $r_e = 6\ \mu$m.

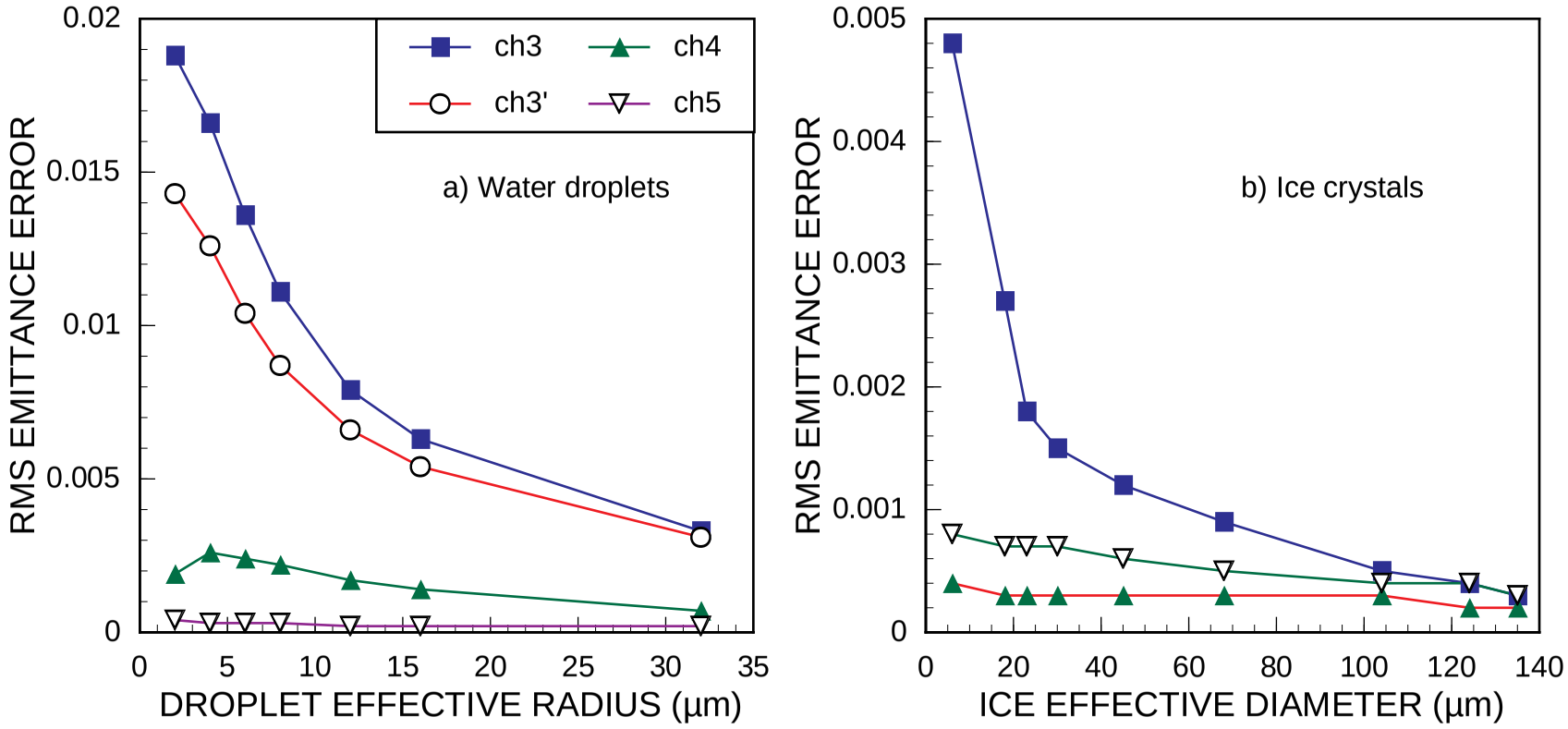

Fig. 13. Emittance parameterization errors. Ch3' refers to errors for emittances less than 1 only.

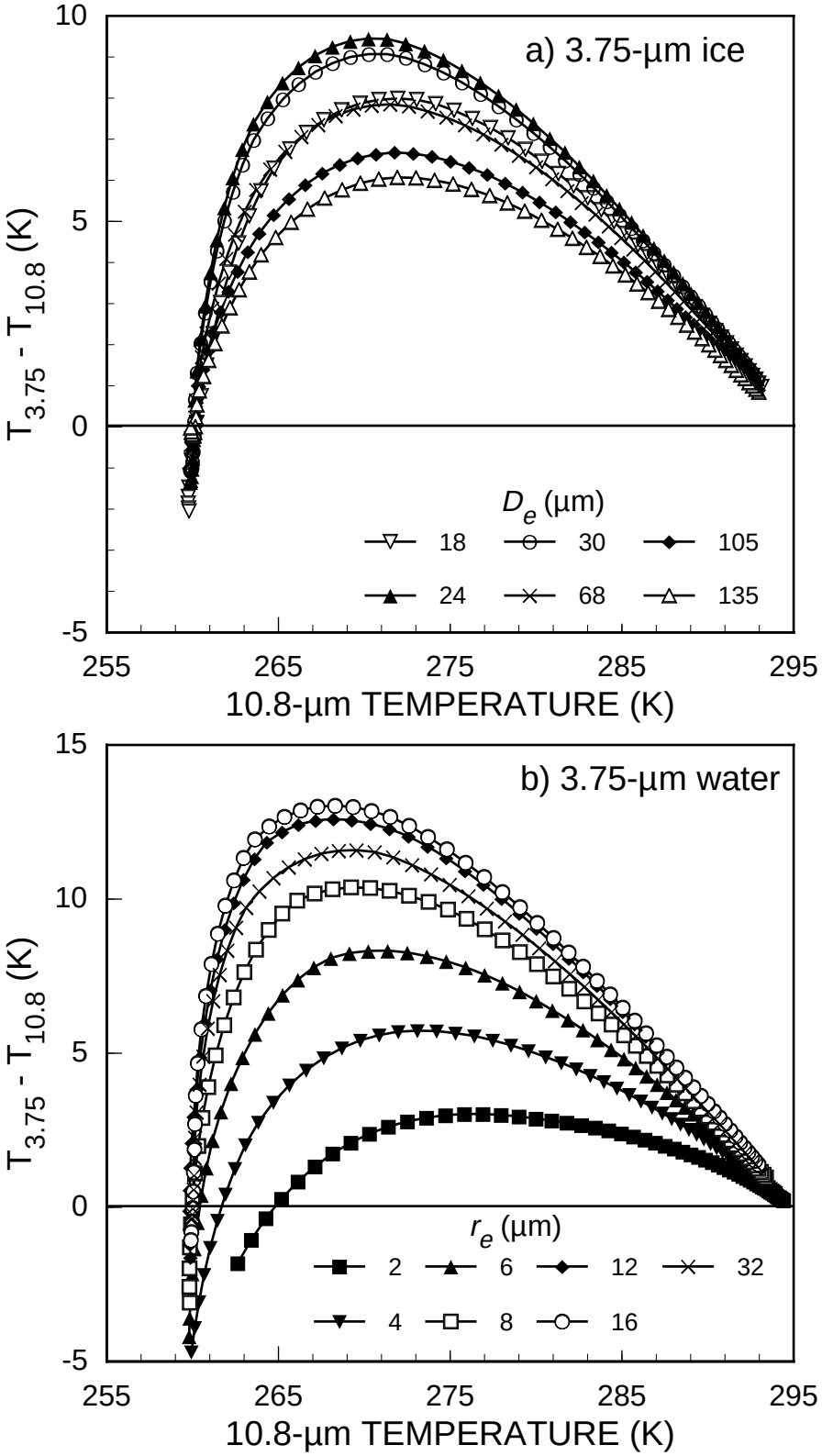

Fig. 14. Brightness temperature differences from parameterizations for T_s = 295 K, T_c = 260 K, $\tau < 16$, and $\theta = 30°$.

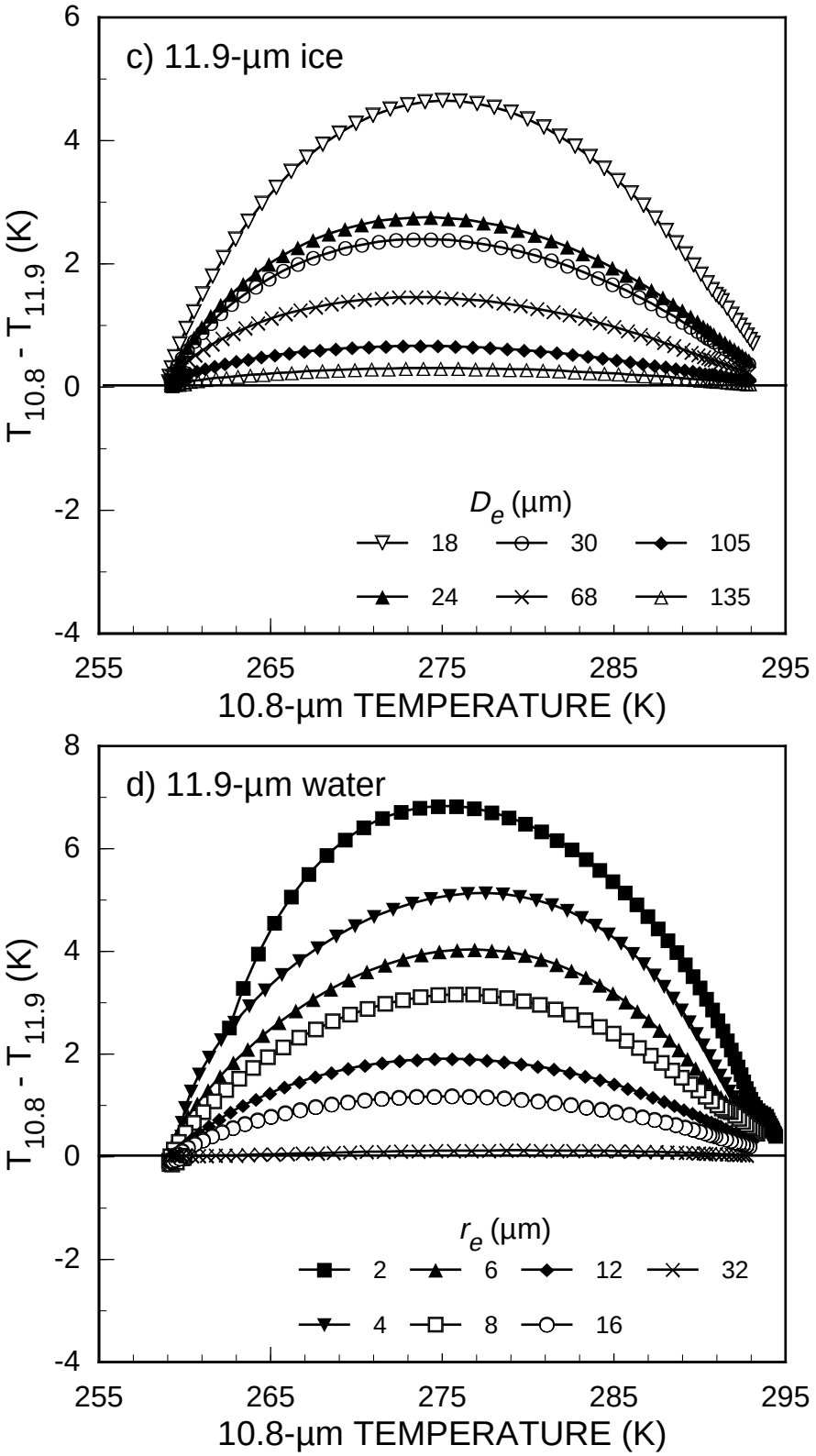

Fig. 14. Continued

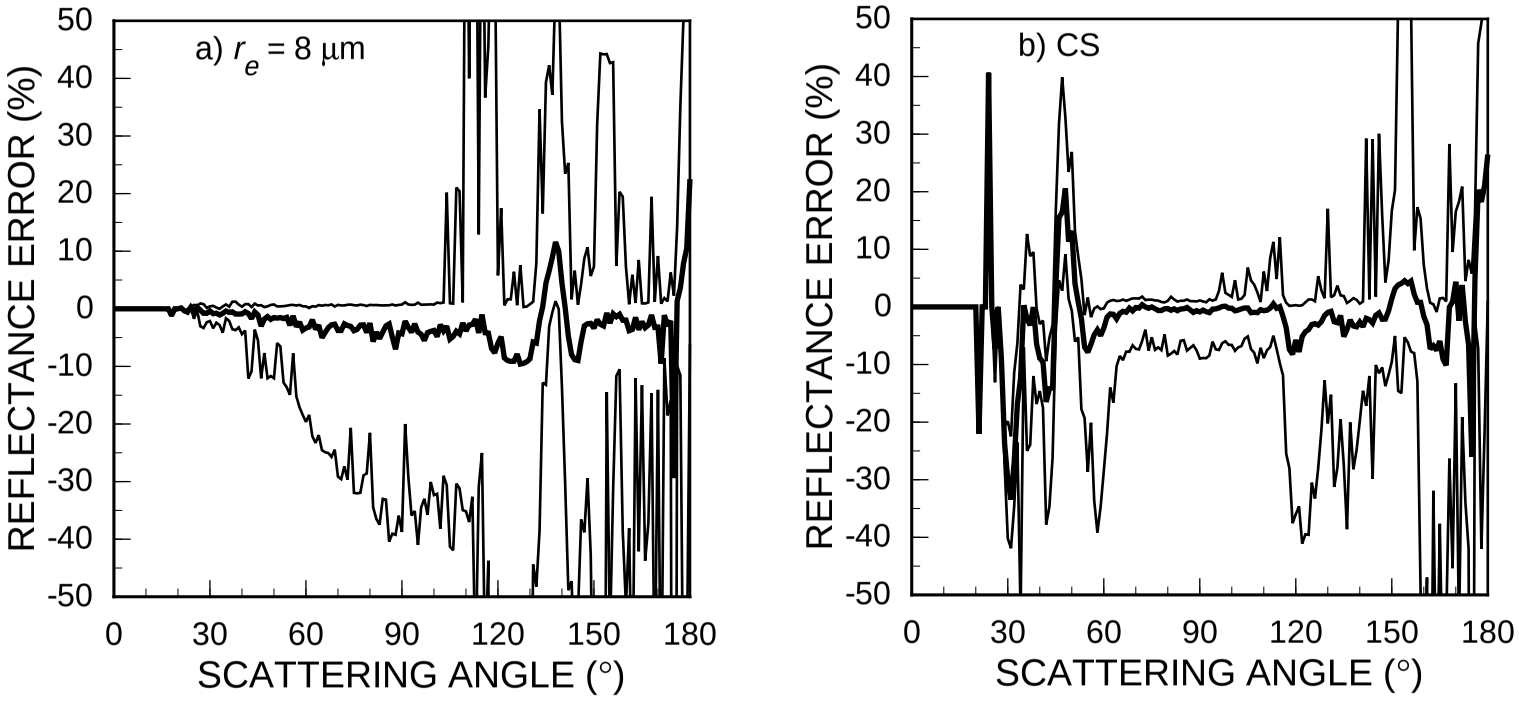

Fig. 15. Reflectance errors relative to AD calculations due to interpolation of model lookup tables. Thin lines indicate extreme errors; thick lines denote means at a given scattering angle.

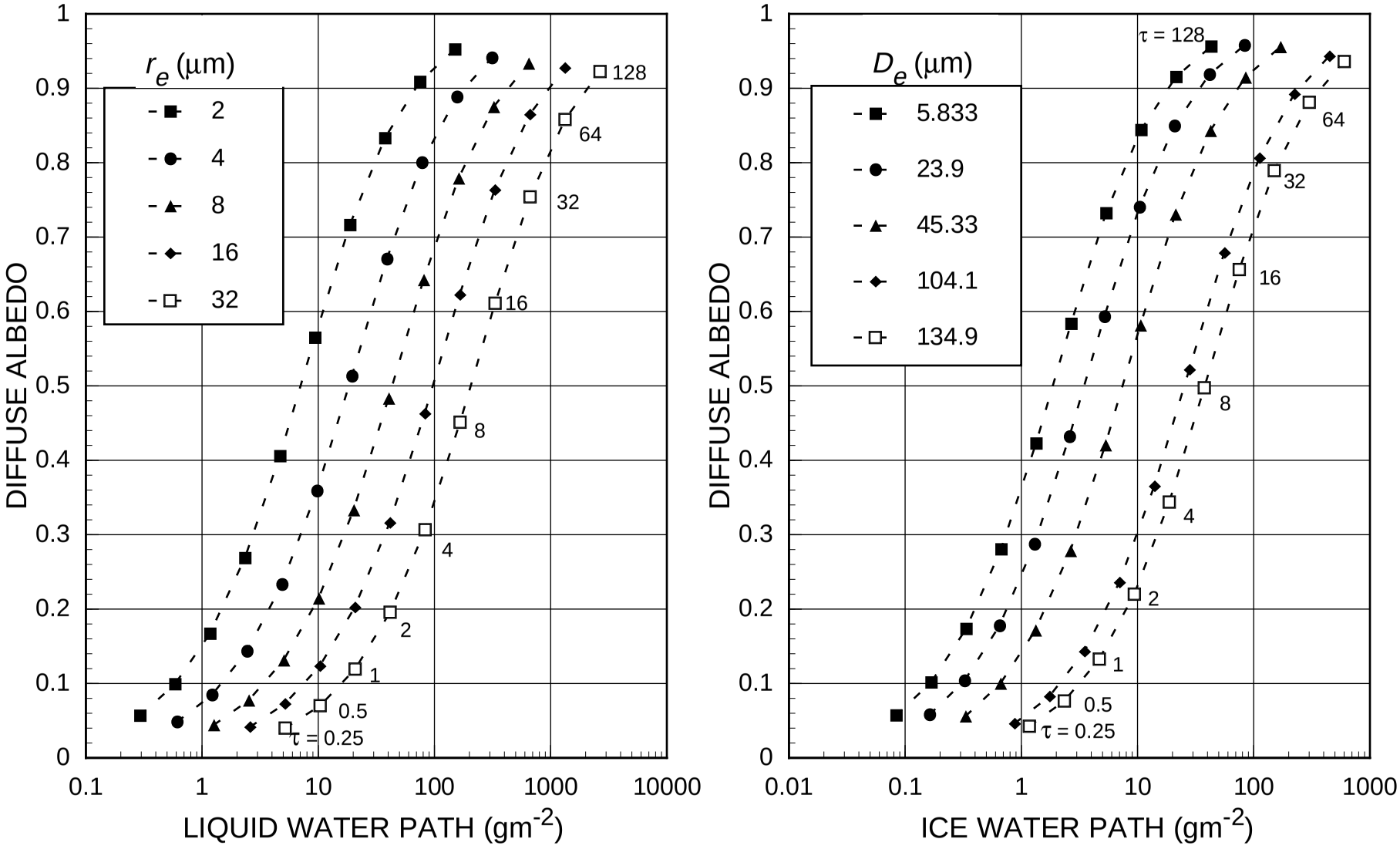

Fig. 16. Spherical albedo as a function of water path for model clouds.

Fig. 17. Cirrus clouds over the Coral Sea observed with NOAA-11 AVHRR 4-km data at 0511 UTC, January 17, 1993.

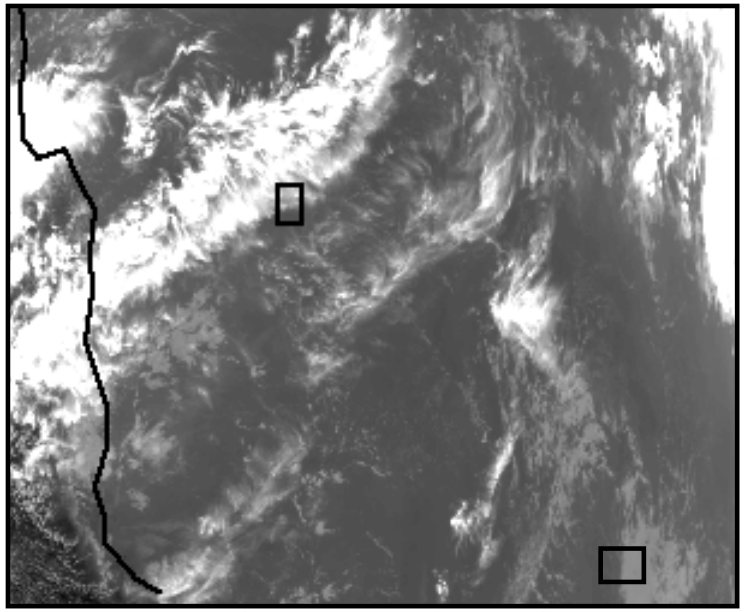

a) IR image with cirrus (top) and stratus (bottom) regions denoted with rectangles

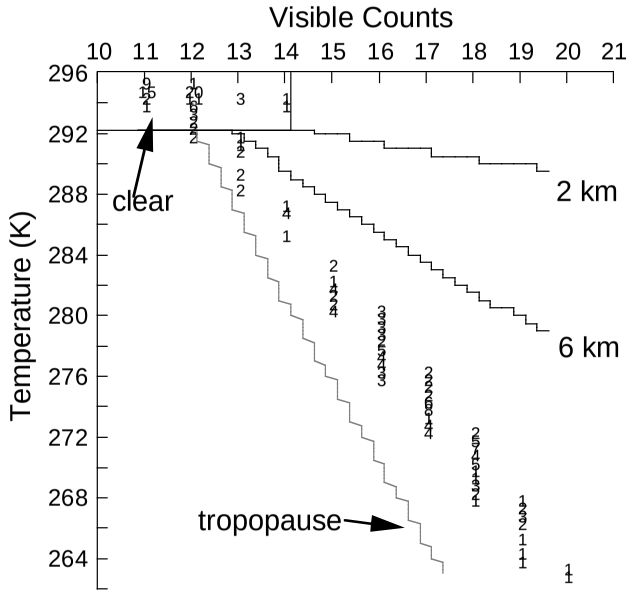

b) Histogram of 8-bit visible counts and IR temperatures for cirrus region

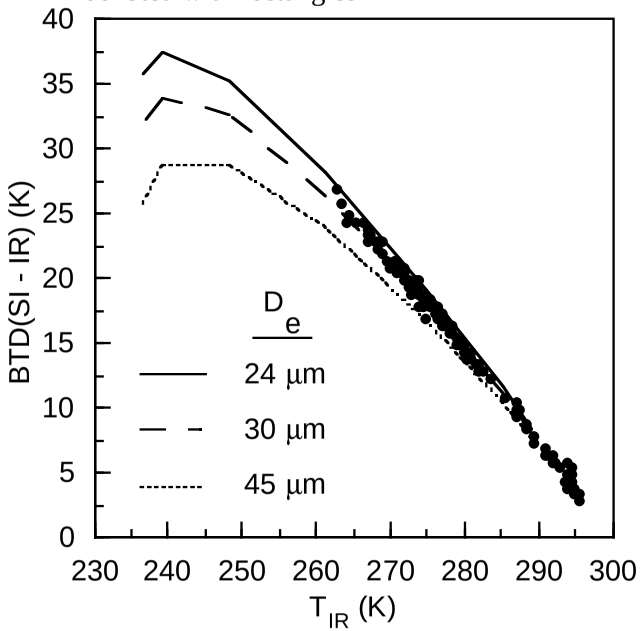

c) SI-IR temperature differences with overlaid ice model results

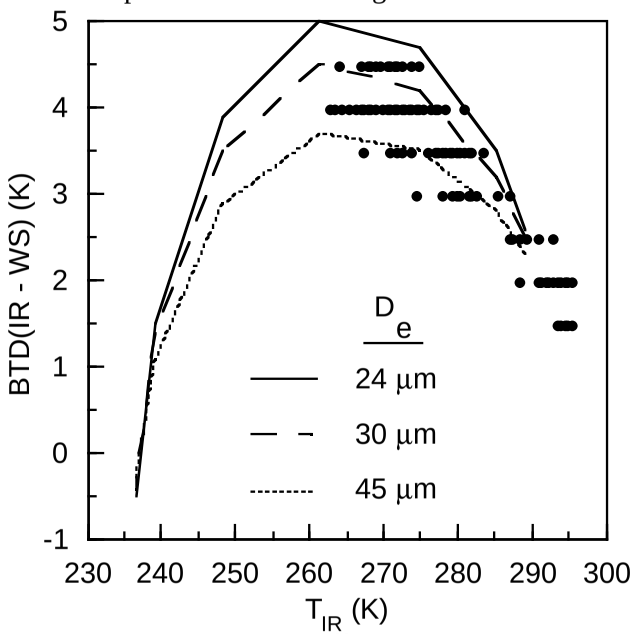

d) IR-WS temperature differences with overlaid ice model results

Fig. 18. Same as Fig. 17, except for stratus clouds as indicated in bottom of Fig. 17a.

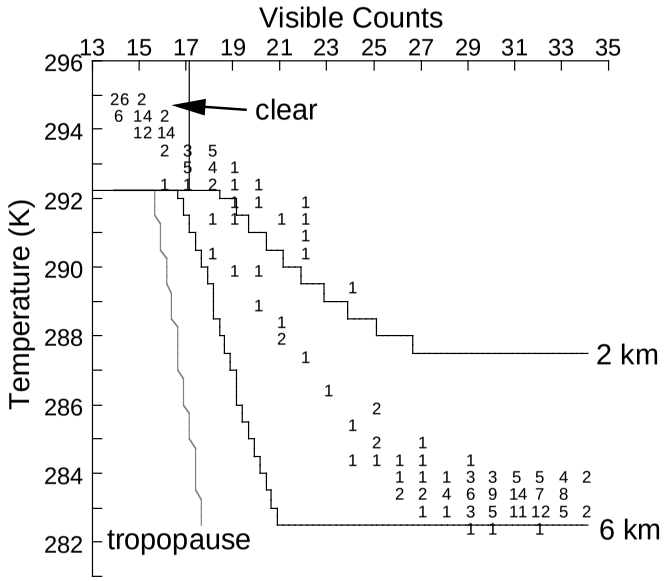

a) Histogram of 8-bit visible counts and IR temperatures for stratus region

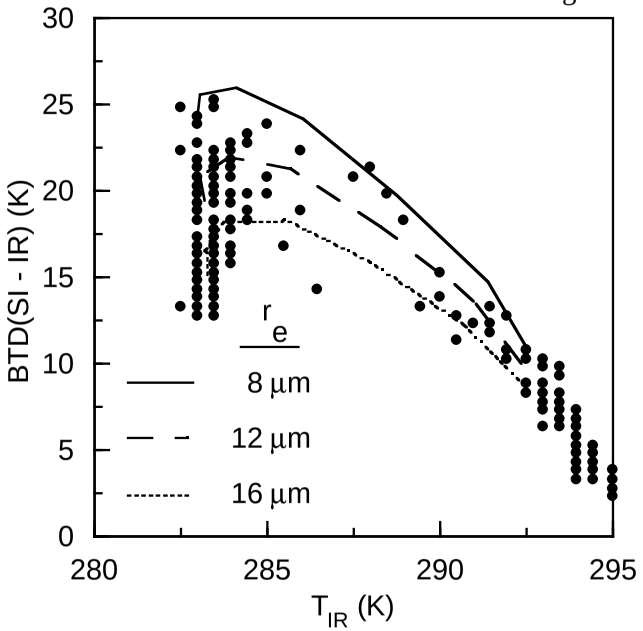

b) SI-IR temperature differences with overlaid water-droplet model results

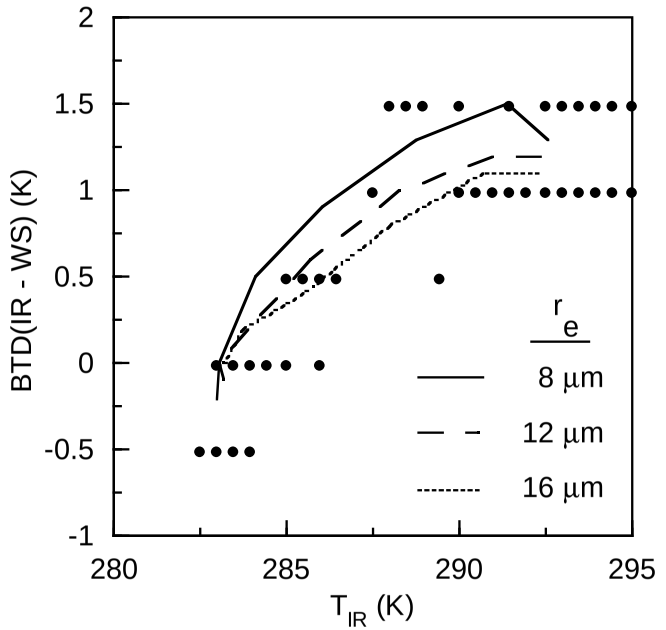

c) IR-WS temperature differences with overlaid water-droplet model results

Fig. 18. Same as Fig. 17, except for stratus clouds as indicated in bottom of Fig. 17a.

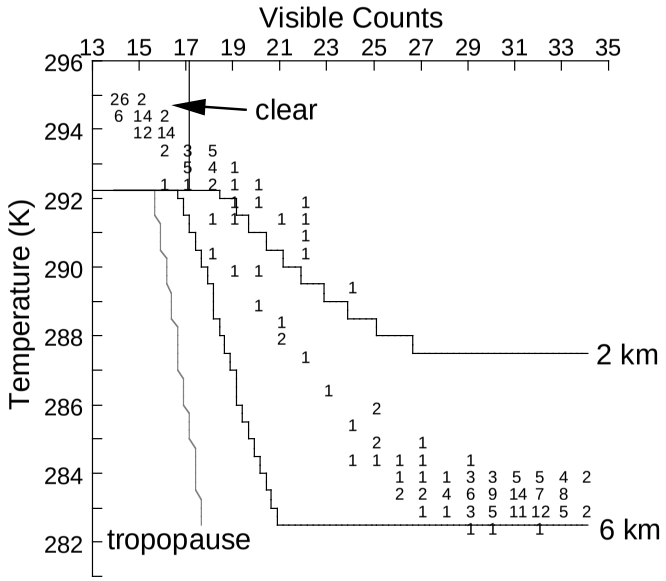

a) Histogram of 8-bit visible counts and IR temperatures for stratus region

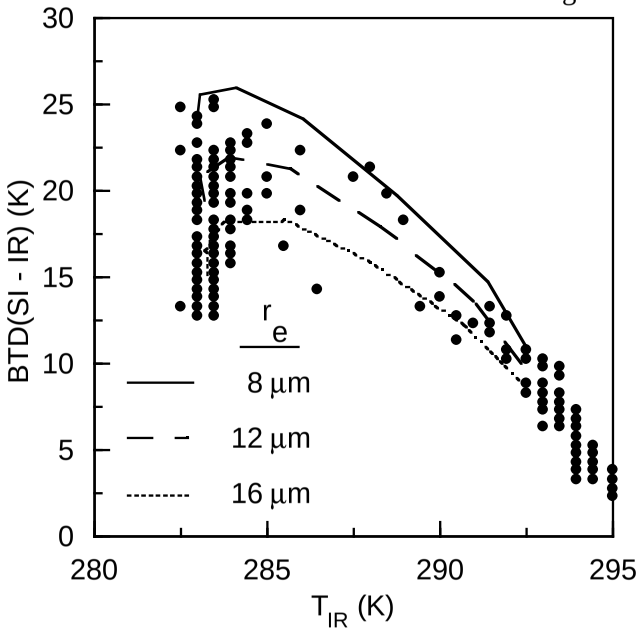

b) SI-IR temperature differences with overlaid water-droplet model results

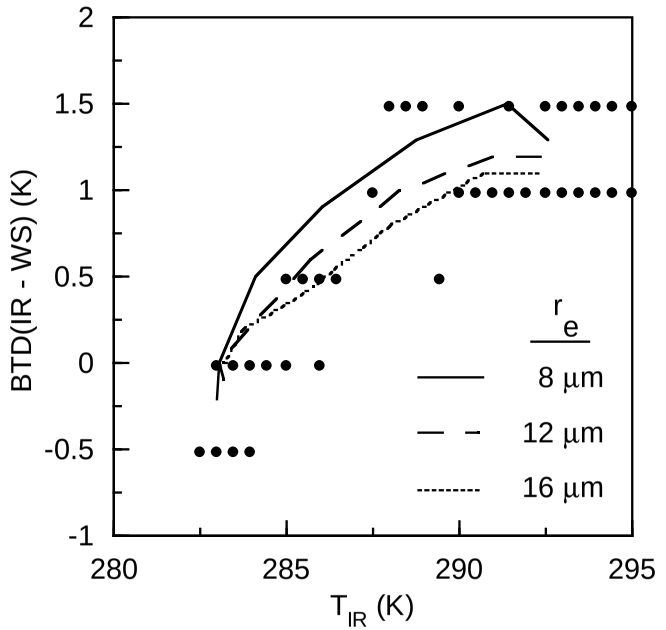

c) IR-WS temperature differences with overlaid water-droplet model results

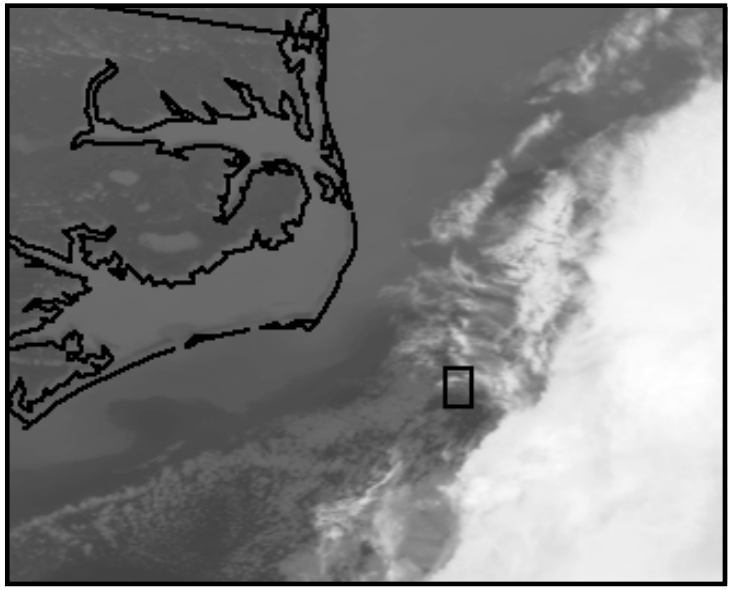

a) IR image

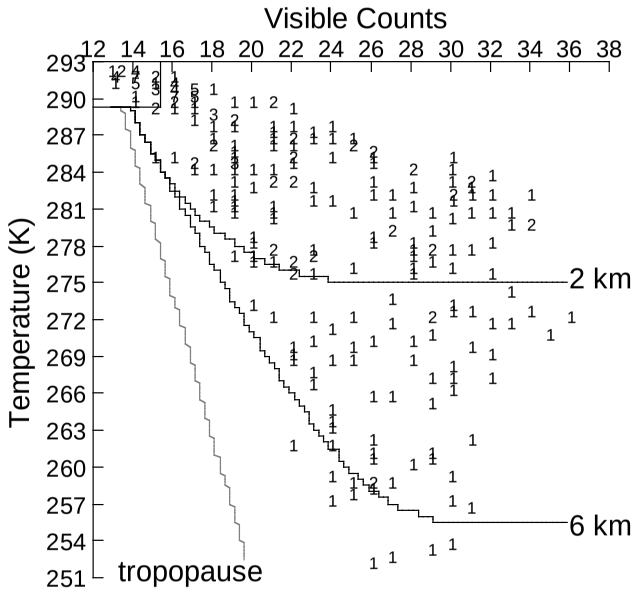

b) VIS-IR histogram for region outlined by rectangle

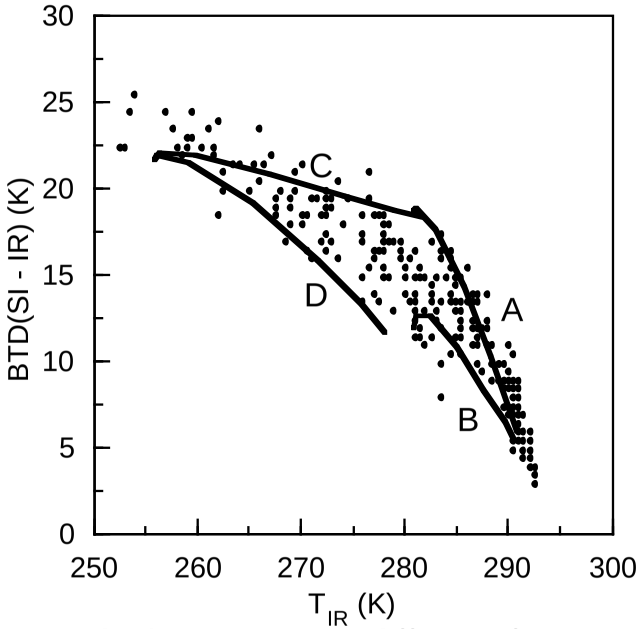

c) SI-IR brightness temperature differences for region in rectangle with overlaid model results

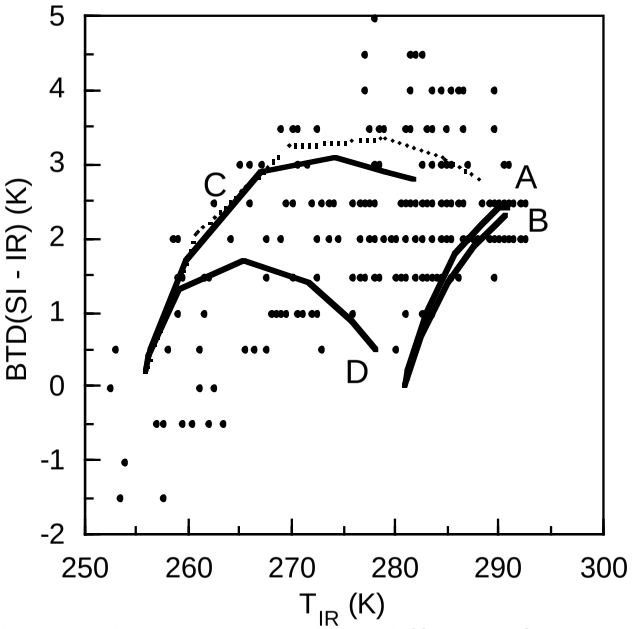

d) IR-WS brightness temperature differences for region in rectangle with overlaid model results

Fig. 19. Multilevel cirrus and stratocumulus clouds east of Cape Hatteras, N. C. observed with NOAA-14 AVHRR 1-km data at 1848 UTC, January 16, 1997. A: T_c = 281 K, r_e = 8 μm; B: T_c = 281 K, r_e = 12 μm; C: T_s = 285 K, T_c = 256 K, D_e = 30 μm; D: T_s = 285 K, T_c = 256 K, D_e = 30 μm; dashed line - T_s = 292 K, T_c = 256 K, D_e = 30 μm.

Fig. 20. Contrail cloudiness over the coast of Virginia observed with NOAA-12 AVHRR 1-km data at 1214 UTC, September 26, 1996.

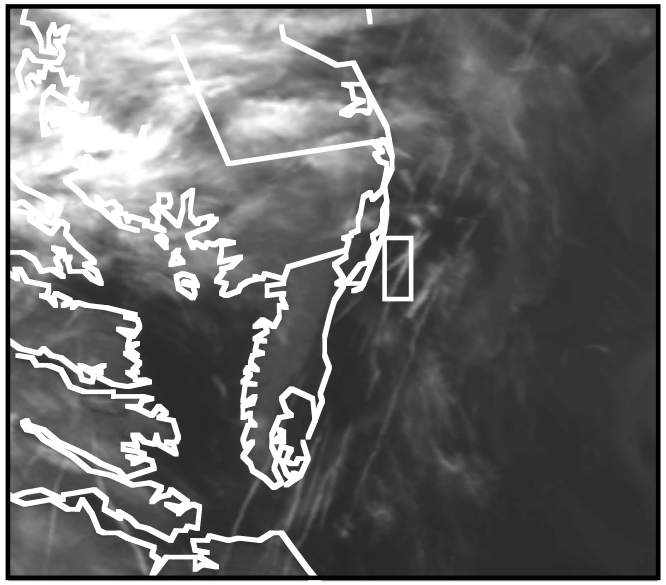

a) IR image with analysis region outlined by rectangle

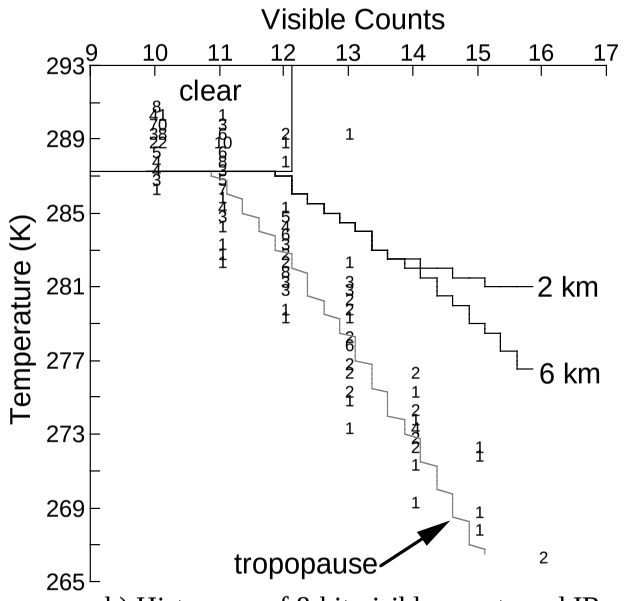

b) Histogram of 8-bit visible counts and IR temperatures for outlined region

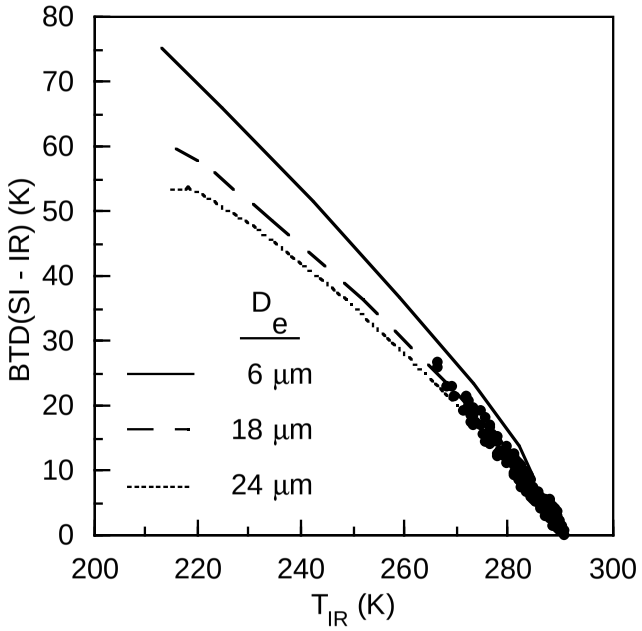

c) SI -IR temperature differences with overlaid ice model results

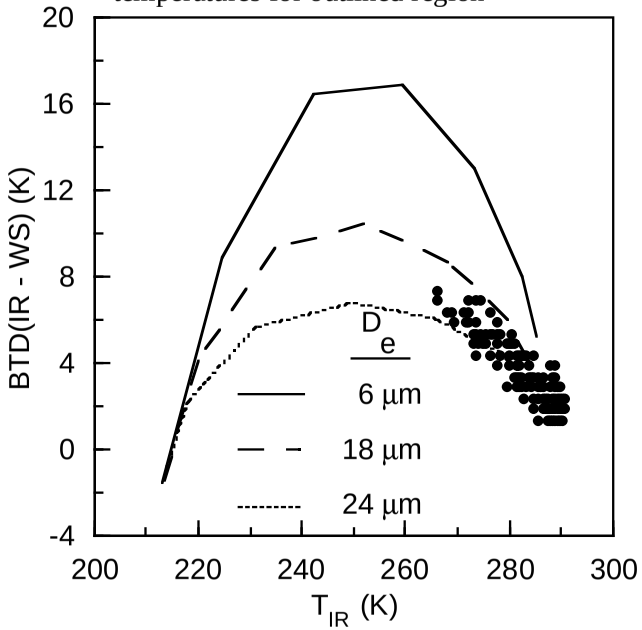

d) IR-WS temperature differences with overlaid ice model results

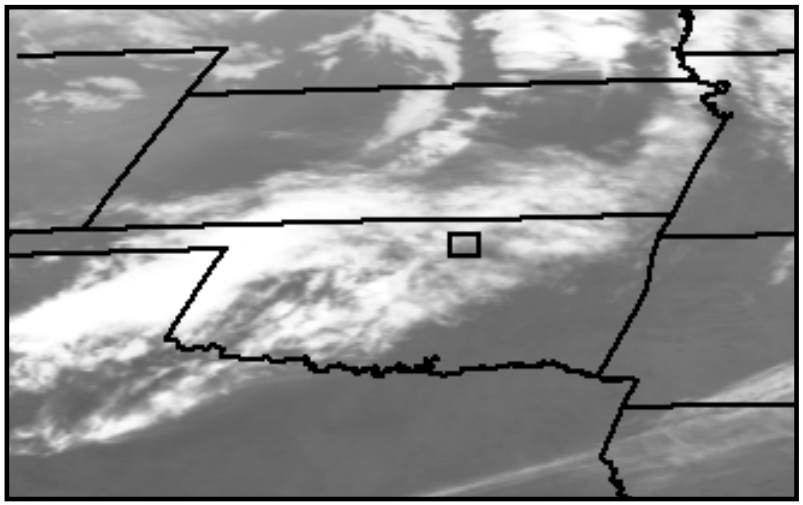

a) IR image showing region outlined with rectangle

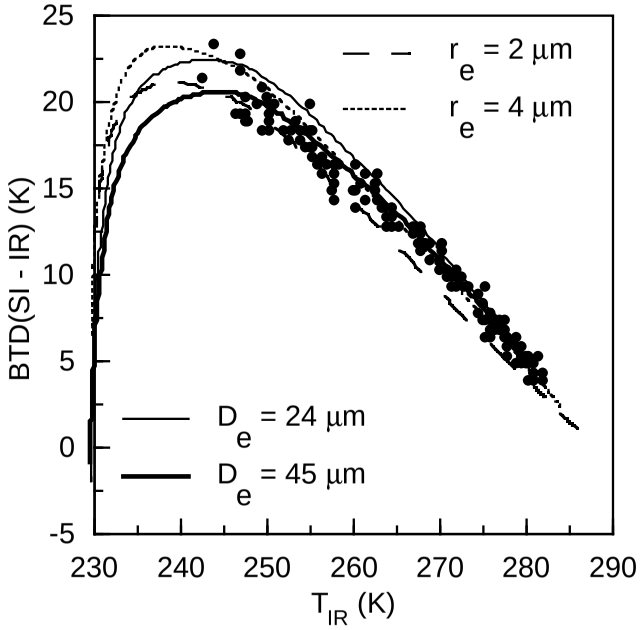

b) SI-IR brightness temperature differences with overlaid parameterization results

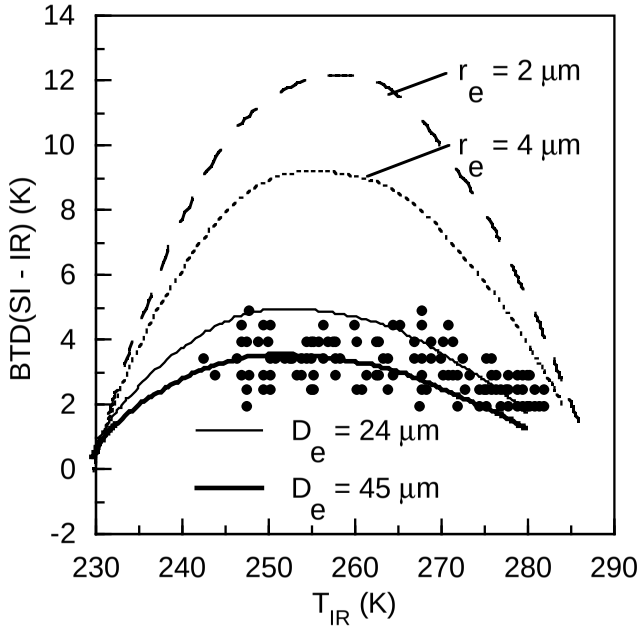

c) IR-WS brightness temperature differences with overlaid parameterization results

Fig. 21. Cirrus clouds over ARM Southern Great Plains Central Facility observed with GOES-8, 4-km data at 0145 UTC, April 15, 1995.

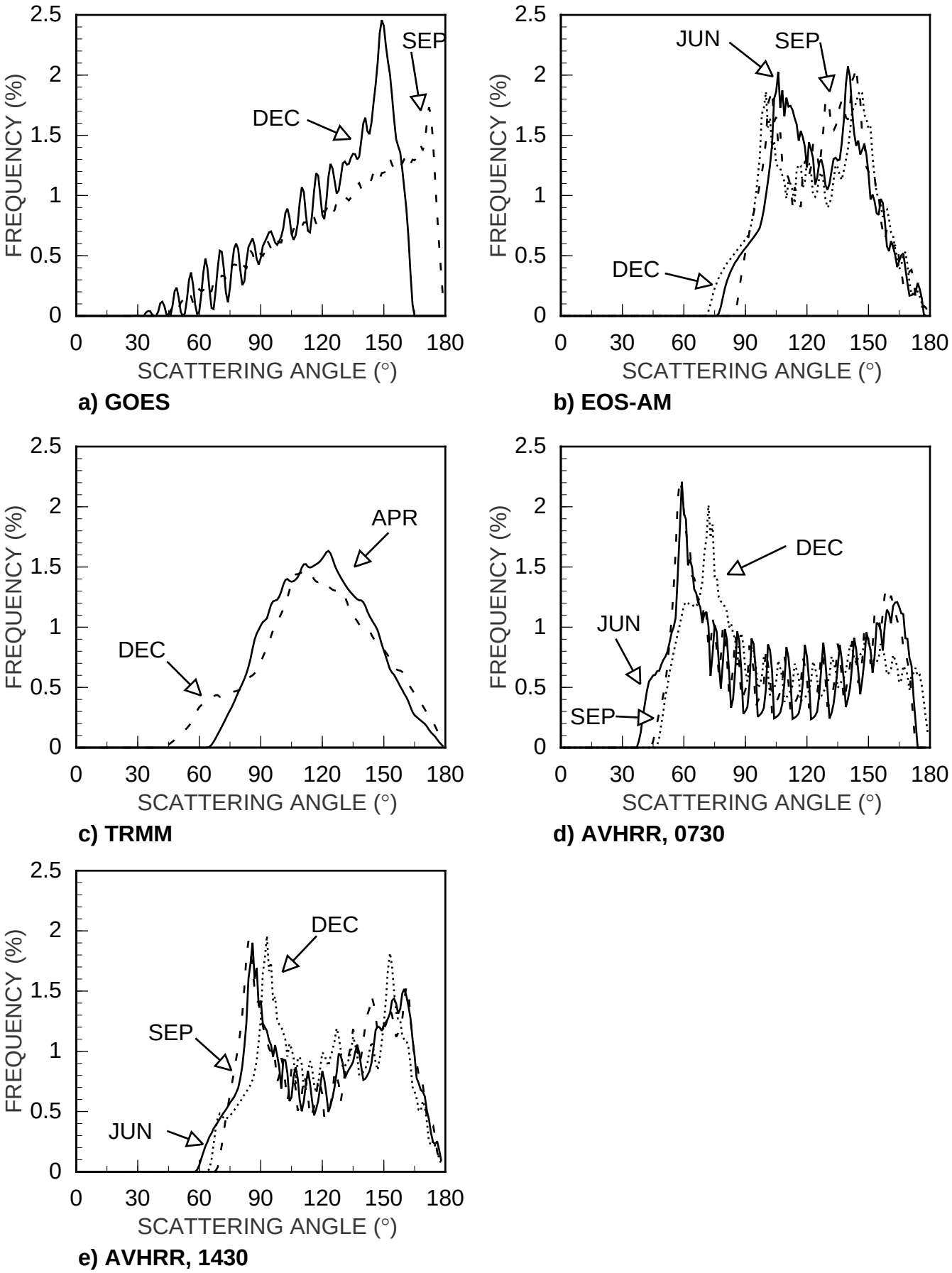

Fig. A1. Scattering angles observed by various satellites for $\theta_o < 82°$, $\theta < 70°$.

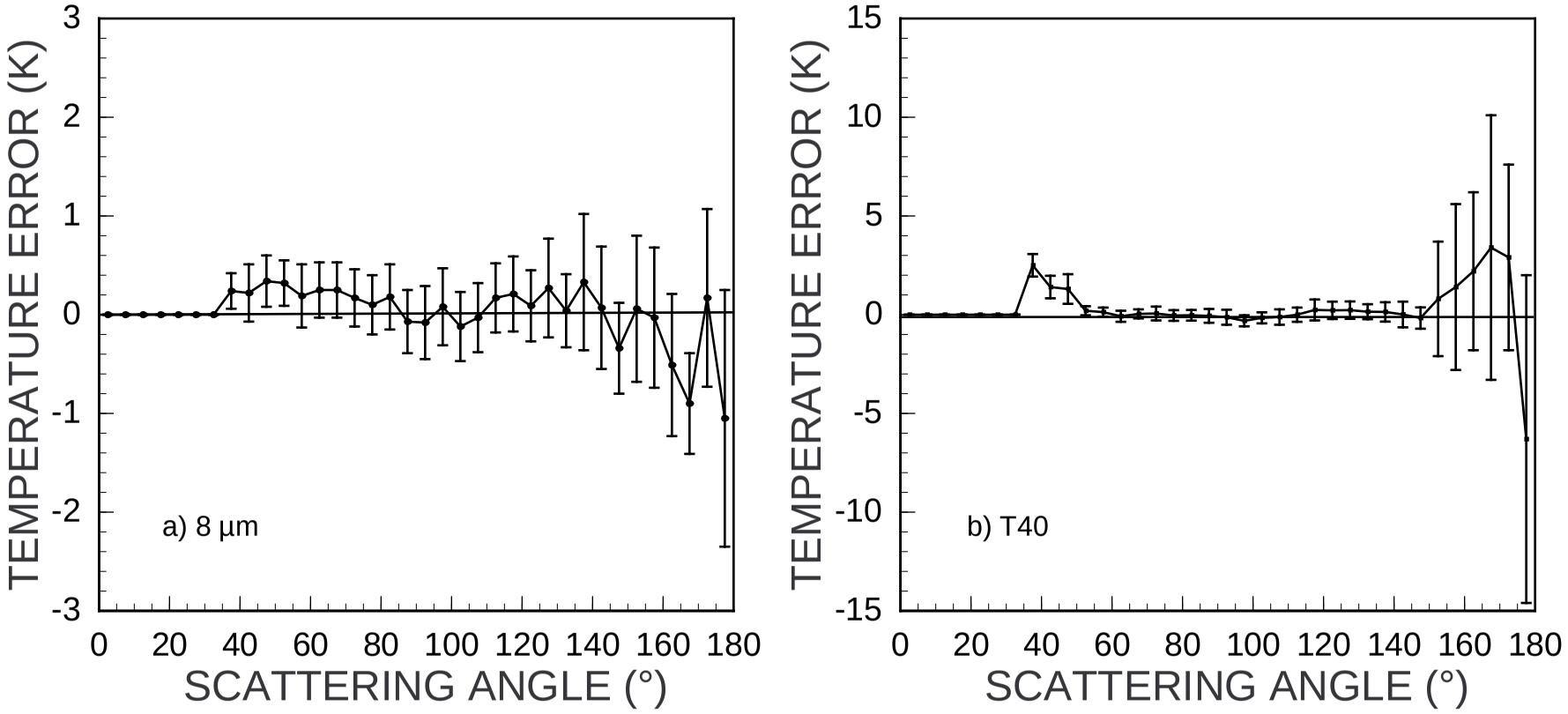

Fig. A2. Scattering angle dependence of errors in 3.75-μm equivalent blackbody temperatures at the top of the atmosphere relative to adding-doubling computations for two different cloud models.